

Obscured AGN and the X-ray, Optical and Far-Infrared Number Counts of AGN in the GOODS Fields

Ezequiel Treister^{1,2}, C. Megan Urry¹, Eleni Chatzichristou¹, Franz Bauer³, David M. Alexander³, Anton Koekemoer⁴, Jeffrey Van Duyne¹, William N. Brandt⁵, Jacqueline Bergeron⁶, Daniel Stern⁷, Leonidas A. Moustakas⁴, Ranga-Ram Chary⁸, Christopher Conselice⁹, Stefano Cristiani¹⁰, Norman Grogin¹¹

treister@astro.yale.edu

ABSTRACT

The deep X-ray, optical, and far-infrared fields that constitute GOODS are sensitive to obscured AGN ($N_H \gtrsim 10^{22} \text{ cm}^{-2}$) at the quasar epoch ($z \sim 2 - 3$), as well as to unobscured AGN as distant as $z \sim 7$. Luminous X-ray emission is a sign of accretion onto a supermassive black hole and thus reveals all but the most heavily obscured AGN. We combine X-ray luminosity functions with appropriate spectral energy distributions for AGN to model the X-ray, optical and far-infrared flux distributions of the X-ray sources in the GOODS fields. A simple model based on the unified paradigm for AGN, with ~ 3 times as many obscured AGN as unobscured, successfully reproduces the z -band flux distributions measured in

¹Yale Center for Astronomy & Astrophysics, Yale University, P.O. Box 208121, New Haven, CT 06520

²Departamento de Astronomía, Universidad de Chile, Casilla 36-D, Santiago, Chile.

³Institute of Astronomy, Madingley Road, Cambridge CB3 0HA, UK.

⁴Space Telescope Science Institute, 3700 San Martin Drive, Baltimore, MD 21218.

⁵Department of Astronomy and Astrophysics, Pennsylvania State University, 525 Davey Laboratory, University Park, PA 16802.

⁶Institut d'Astrophysique de Paris, 98bis Boulevard Arago, F-75014 Paris, France.

⁷Jet Propulsion Laboratory, California Institute of Technology, Mail Stop 169-506, Pasadena, CA 91109.

⁸SIRTF Science Center, California Institute of Technology, MS 220-6, Pasadena, CA 91125.

⁹California Institute of Technology, Pasadena, CA 91125.

¹⁰INAF-Osservatorio Astronomico, Via Tiepolo 11, I-34131 Trieste, Italy.

¹¹Department of Physics and Astronomy, Johns Hopkins University, 3400 North Charles St., Baltimore, MD, 21218.

the deep HST ACS observations on the GOODS North and South fields. This model is also consistent with the observed spectroscopic and photometric redshift distributions once selection effects are considered. The previously reported discrepancy between observed spectroscopic redshift distributions and the predictions of population synthesis models for the X-ray background can be explained by bias against the most heavily obscured AGN generated both by X-ray observations and the identification of sources via optical spectroscopy. We predict the AGN number counts for *Spitzer* MIPS 24 μm and IRAC 3.6-8 μm observations in the GOODS fields, which will verify whether most AGN in the early Universe are obscured in the optical. Such AGN should be very bright far-infrared sources and include some obscured AGN missed even by X-ray observations.

Subject headings: galaxies: active, quasars: general, X-rays: diffuse background

1. Introduction

Extensive studies of local Active Galactic Nuclei (AGN) have led to a unification paradigm wherein continuum and broad-line emission from the active nucleus are hidden from some lines of sight by an optically thick medium (Antonucci 1993). At such orientations, AGN lack broad emission lines or a bright continuum and are called Type 2 AGN (e.g., Seyfert 2 galaxies); usually they have strongly absorbed X-ray spectra as well. A population of these obscured AGN out to redshift 2-3 has been invoked to explain the X-ray “background” (Madau, Ghisellini, & Fabian 1994; Comastri et al. 1995). Recent deep surveys with *Chandra* and XMM have resolved most or all of this background, and thus must contain high-redshift, obscured AGN (Brandt et al. 2001; Rosati et al. 2002). Obscured AGN are needed to explain the spectral shape of the X-ray background (Setti & Woltjer 1989) since the average observed AGN spectrum (Gruber 1992) is much harder than the typical X-ray spectrum of an unobscured AGN (Mushotzky et al. 1993). Because strong absorption of the ultraviolet and soft X-ray emission dramatically hardens the observed spectrum of obscured AGN, population synthesis models involving large numbers of obscured AGN have been very successful at matching the X-ray background intensity and spectrum (e.g., Madau, Ghisellini, & Fabian 1994; Comastri et al. 1995; Gilli et al. 1999, 2001).

The main prediction of population synthesis models, namely that a combination of obscured and unobscured AGN constitute the X-ray background, has been borne out by deep X-ray observations (Gilli 2003; Perola et al. 2004). However, the observed redshift distribution of X-ray sources in deep surveys is peaked at lower redshift than these models require. Specifically, Gilli et al. (2001) predict a peak in the redshift distribution at $z \sim 1.4$,

and a ratio of obscured to unobscured AGN that rises from 4:1 locally to 10:1 at $z \simeq 1.3$. However, optical spectroscopy of X-ray sources in the *Chandra* Deep Fields and the Lockman Hole indicates a redshift peak at $z \simeq 0.7$, and only twice as many obscured AGN as unobscured (Hasinger 2002; Barger et al. 2003).

Because few Type 2 AGN are known at redshifts $z \sim 2 - 3$, where AGN are most numerous, it had been suggested that they do not exist, perhaps because the obscuring torus of gas and dust evaporates at high luminosity (Lawrence 1987). Now, with deep X-ray surveys, a few such objects have clearly been found (e.g., Norman et al. 2002; Stern et al. 2002; Dawson et al. 2003). It is important to note that UV-excess or optical emission-line surveys would not have found most obscured AGN, nor would soft X-ray surveys such as the ROSAT All-Sky (Voges et al. 1999) or the White, Giommi & Angelini (WGA; Singh et al. 1995) surveys. Instead, one needs to look at hard X-rays, where the absorption is smaller, or in the far infrared, where the absorbed energy is re-radiated.

Discovering a previously undiscovered population of obscured AGN — a population suggested by the hardness of the X-ray background — was a strong motivation for the Great Observatories Origins Deep Survey. GOODS consists of deep imaging in the far infrared with the *Spitzer* Space Telescope (Dickinson & Giavalisco 2002) and in the optical with the Hubble Space Telescope (Giavalisco et al. 2004) on the footprints of the two deepest *Chandra* fields (Giacconi et al. 2001; Brandt et al. 2001; Alexander et al. 2003, hereafter A03). The total area is roughly 60 times larger than the original Hubble Deep Field (Williams et al. 1996) and nearly as deep in the optical. The Great Observatories data were augmented with ground-based imaging and spectroscopy¹. With extensive coverage over 5 decades in energy from 24 μm to 8 keV ($\lambda = 1.55 \text{ \AA}$), this survey is well suited to find a high-redshift population of obscured AGN if they exist. A complementary approach, given the relatively low surface density of AGN (compared to normal galaxies), is to target higher luminosity AGN over a wider area of the sky, an approach followed by, for example, the Chandra Multiwavelength Project (ChAMP; Green et al. 2004), Calan-Yale Deep Extragalactic Research (CYDER; Castander et al. 2003), Serendipitous Extragalactic X-ray source identification program (SEXSI; Harrison et al. 2003) and the High-Energy Large-Area Survey 2 (HEL-LAS2XMM; Baldi et al. 2002) surveys.

In this paper we discuss the AGN populations detected in the X-ray and optical in the GOODS North and South fields. Assuming a simple unification scheme, in which roughly three-quarters of all AGN are obscured at all redshifts, we explain the optical magnitude, hard X-ray flux, and redshift distributions of GOODS AGN. This model is compatible with

¹Observations are summarized at <http://www.stsci.edu/science/goods/>

previous population syntheses models for the X-ray background. We also use this model to predict the number counts and redshift distribution of AGN that will be detected with *Spitzer* in the GOODS fields. These predictions differ from similar calculations by Andreani et al. (2003) in that we include AGN evolution, which has a very strong effect, changing the counts by 2 orders of magnitude at the wavelengths of interest.

In § 2 we outline the procedure used to derive the number counts and redshift distributions at various wavelengths, and specify the AGN luminosity function and Spectral Energy Distributions used, which are appropriate to the unification paradigm and are based on a combination of observation and theory. Results are discussed in § 3, and compared to observations in the GOODS fields. In § 4 we present predictions for the *Spitzer* observations at 24, 8 and 3.6 microns and discuss definitive tests for the obscured population. Conclusions are given in § 5. Throughout this paper we assume $H_0 = 70 \text{ km s}^{-1} \text{ Mpc}^{-1}$, $\Omega_m = 0.3$ and $\Omega_\Lambda = 0.7$.

2. Calculation of Multiwavelength Number Counts

2.1. Overview of Inputs and Procedure

To derive the number counts at any wavelength we start with a hard X-ray luminosity function, an assumed cosmic evolution, and a library of spectral energy distributions. We use the hard X-rays as a starting point because observations at 2-10 keV in the rest frame are less affected by obscuration and therefore provide a less biased view of the AGN population, although they are still biased against detection of heavily absorbed sources ($N_H \gtrsim 10^{23} \text{ cm}^{-2}$). The intrinsic X-ray luminosity of each AGN is then related to its observed X-ray flux via its N_H value and intrinsic X-ray spectral index.

Hard X-ray surveys are heavily dominated by AGN and thus make AGN very easy to identify. Although far-infrared emission can be even less biased, since the optical depth of the obscuring matter is low and the dust emission is quasi-isotropic (Pier & Krolik 1992), such surveys have a very low yield of AGN because normal galaxies are also strong far-infrared sources and are far more numerous.

Hard X-ray luminosity functions based on compilations of deep *Chandra*, ROSAT, HEAO-1 and ASCA observations have been published recently by Ueda et al. (2003;U03 in what follows) and Steffen et al. (2003). We use the work of U03, based on 247 AGN selected in the hard X-ray band in deep fields like the Lockman Hole and the *Chandra* Deep Field North. This sample covers the X-ray flux range from 10^{-10} to $3.8 \times 10^{-15} \text{ erg cm}^{-2} \text{ s}^{-1}$ in the 2–10 keV band. The luminosity function refers to the rest-frame absorption-corrected X-ray

luminosity. The dependence of the luminosity function on the column density is calculated separately using an “ N_H function” presented in Equation 6 of U03, which is based on the relative number of sources at each N_H observed in their sample.

The number of sources per unit volume per unit of $\log L_X$ and per unit of $\log N_H$ is (U03):

$$\frac{d^3 N(N_H, L_X, z)}{dN_H dL_X dz} = f(L_X, z; N_H) \frac{d\Phi(L_X, z)}{d \log L_X} V(z), \quad (1)$$

where Φ is the luminosity function, which also includes evolution with redshift, f is the observed neutral hydrogen column density distribution and $V(z)$ is the co-moving volume as a function of redshift, which depends on the adopted cosmology. We also adopt the luminosity-dependent density evolution model of U03, in which low-luminosity sources peak at lower redshift than high-luminosity AGN. This is compatible with evolution calculated in the optical bands by Boyle et al. (2000), which peaks at redshift $z \sim 2$ (but includes only high luminosity objects). We refer the reader to U03 for more details about the hard X-ray luminosity function.

The Spectral Energy Distributions (SEDs) described in § 2.2 give the AGN luminosity at any wavelength. We use the number density in Eqn. (1) to generate a population of objects spanning the following ranges of L_X and N_H : $N_H = 10^{20} - 10^{24} \text{ cm}^{-2}$ and $L_X = 10^{42} - 10^{48} \text{ ergs s}^{-1}$. We calculate the number counts at any given wavelength by summing sources of the same observed flux at that wavelength, and scaling the result to the total area. We book keep this calculation separately for different populations, for example, unobscured and obscured AGN, adopting $N_H = 10^{22} \text{ cm}^{-2}$ as the dividing point between the two classes (as do U03).

The combination of the U03 luminosity function (version appropriate for our cosmology; see Table 3 in U03), N_H function, and the AGN SEDs described in the next section will be called Model A in what follows.

2.2. AGN Spectral Energy Distributions

The rest-frame spectrum of an AGN depends strongly on the intrinsic luminosity of the central engine and the amount of obscuration along the line of sight. In the simple unification model considered here, the obscuring matter is distributed in an axially symmetric geometry which, assuming random orientations of the symmetry axis, dictates the distribution of neutral hydrogen column density, N_H . The obscuring gas and dust both absorbs and emits

radiation (Nenkova et al. 2002; Elitzur et al. 2003; see also Pier & Krolik 1992, 1993; Granato & Danese 1994), conserving energy when integrated over all angles.

We construct AGN SEDs from X-rays to the far infrared as a function of two parameters, namely the intrinsic X-ray luminosity in the 2-10 keV band and the line-of-sight column density of neutral hydrogen, N_H . We consider three separate wavelength regions — X-rays, optical/UV, and infrared — then merge the components with appropriate normalizations. Specifically the SEDs are constructed as follows:

- The intrinsic relation between X-ray and UV luminosity (Vignali et al. 2003) was used to normalize the unobscured optical AGN spectrum, which is taken from the SDSS composite quasar spectrum (Vanden Berk et al. 2001).
- Absorption was then added to both the X-ray and UV/optical parts of the spectrum. In X-rays photoelectric absorption was assumed, while in the UV/optical Milky-Way type reddening laws were used, with a standard galactic dust-to-gas ratio to convert N_H into optical extinction (see § 2.2.1 and 2.2.2 for details).
- An L_* ($M_B = -20.47$ mag) elliptical host galaxy was added to the optical AGN spectrum. In the most obscured sources, the host galaxy dominates the rest-frame optical-near-IR spectrum. See § 2.2.2 for details.
- The value of N_H for the infrared dust emission models of Nenkova et al. (2002); Elitzur et al. (2003) was related to the angle between the equatorial plane of the AGN and the line of sight for a simple torus geometry (§ 2.2.3).
- The infrared spectra for different angles are normalized at $100\mu\text{m}$, where the emission from the AGN is roughly isotropic (Pier & Krolik 1992), and the infrared spectrum for the appropriate angle (i.e., N_H value) is added to the AGN spectrum. Details are presented in § 2.2.3.

This composite spectrum is shifted to the desired redshift and the change in the SED of the host galaxy caused by passive stellar evolution is included (see § 2.2.2).

Examples of the final composite SEDs for some of the X-ray luminosities and N_H values used in this calculation are shown in Figure 1. Two known AGN, the Type 1 quasar PG0804+761 ($z = 0.1$, $N_H = 3.1 \times 10^{20} \text{ cm}^{-2}$; Elvis et al. 1994) and the Seyfert 2 galaxy NGC 7582 ($z = 0.00525$, $N_H = 1.24 \times 10^{23} \text{ cm}^{-2}$; Bassani et al. 1999) agree well with the appropriate model SEDs, as shown in Figure 2. Note that once N_H and redshift (and thus luminosity) are specified, there are no free parameters to adjust the fit to the data.

The effective broad-band power-law spectral slope, α_{ij} , is defined as:

$$\alpha_{ij} = \frac{\log[f_\nu(j)/f_\nu(i)]}{\log[\nu(j)/\nu(i)]}, \quad (2)$$

where f_ν is the rest-frame flux density and ν_i and ν_j are the frequencies of interest. For our spectral models, a source with an unabsorbed X-ray luminosity of 10^{45} ergs s⁻¹ and $N_H = 10^{20}$ cm⁻² has $\alpha_{ox} = -1.73$, while a low-luminosity AGN with $L_X = 10^{42}$ ergs s⁻¹ and mild obscuration, $N_H = 10^{22}$ cm⁻², has $\alpha_{ox} = -1.41$ (taking 2500 Å and 2 keV as the fiducial points). Both values are well within the observed range, while the average of our model distribution is very similar to the average observed values (Vignali et al. 2003).

Similarly, the values of f_X/f_{IR} for these models, adopting the index defined by Barcons et al. (1995), where f_X is rest-frame monochromatic absorbed flux at 5 keV and f_{IR} is 12-micron flux, are $f_X/f_{IR} = 10^{-6}$ for type 1 AGN, and $f_X/f_{IR} = 2.15 \times 10^{-7}$ for type 2 AGN with unabsorbed X-ray luminosity of 5×10^{44} ergs s⁻¹ and $N_H = 3.2 \times 10^{23}$ cm⁻². Again, both indices are similar to measured values for local AGN (Barcons et al. 1995). Whether these SED models remain valid at high redshift is an hypothesis that is effectively being tested by the comparison of predicted and observed number counts.

2.2.1. X-ray Spectrum

Intrinsic AGN X-ray spectra can be represented by attenuated power laws of the form:

$$\frac{dN(E)}{dE} \propto E^{-\Gamma} e^{-\sigma(E)N_H}, \quad (3)$$

where $N(E)$ is the number of photons with energy E ; Γ is the power-law photon index; $\sigma(E)$ represents the cross section for photoelectric absorption of soft X-rays, given by Morrison & McCammon (1983) assuming solar abundance of metals; and N_H is the neutral hydrogen column density along the line of sight, ranging from typical high Galactic latitude values of $N_H = 10^{20}$ cm⁻² to the limit for Compton-thick absorption, $N_H \sim 10^{24}$ cm⁻². A typical value for the intrinsic slope is $\Gamma = 1.9$ (e.g., Nandra & Pounds 1994; Nandra et al. 1997; Mainieri et al. 2002). However, it is important to note that a reflection hump can make the spectrum look harder, closer to $\Gamma = 1.7$ (Akiyama et al. 2003; Mushotzky et al. 1978; Nandra & Pounds 1994). Here we assume $\Gamma = 1.7$; we have verified that the choice of Γ has only a minor effect in our results.

The X-ray spectrum is normalized relative to the optical using the correlation between intrinsic X-ray luminosity at 2 keV and UV emission at 2500 Å, $L_X \propto L_{UV}^{0.75}$ (Vignali et al.

2003). This relation has a dispersion of ± 0.06 in the exponent and is significant at the 7.9σ level when BALQSOs are excluded (they are in any case rare).

2.2.2. Optical Spectrum

From 1000 \AA to $\sim 1 \mu\text{m}$ we use the Sloan Digital Sky Survey (SDSS) composite quasar spectrum (Vanden Berk et al. 2001), which represents an average of over 2000 SDSS quasars with a median redshift $z = 1.253$, covering rest-frame wavelengths from 800 \AA to 8555 \AA at a resolution of $\sim 1 \text{ \AA}$. The intrinsic luminosity of quasars in this sample spans the range from $M_{r'} = -18 \text{ mag}$ to $M_{r'} = -26.5 \text{ mag}$. This spectrum well represents unobscured (type 1) AGN, in which the optical light from the central engine is not absorbed by the dust or gas torus. Given that the SDSS quasar composite includes AGN brighter than the average AGN observed in X-rays, the use of the SDSS composite spectrum may not be realistic; however, it is completely appropriate to our very simple model which assumes the obscuring torus is independent of luminosity or redshift. Furthermore, there are good indications that the optical spectrum of faint quasars is very similar to the spectrum of the average SDSS quasar (Steidel et al. 2002).

To calculate the effects of absorption on the optical and UV spectrum we use the extinction coefficients of Cardelli et al. (1989), obtained from absorption measurements on Milky Way stars. A standard Milky Way dust-to-gas ratio was assumed to convert neutral hydrogen column density into optical extinction: $N_H = 1.96 \times 10^{21} A_V$ (Bohlin et al. 1978). Some studies of the dust-to-gas ratio in AGN point out that this ratio is on average significantly smaller than the value obtained for the Milky Way (Maiolino et al. 2001b,a), but this picture has been questioned (Weingartner & Murray 2002). Here we assume the more conservative position and use the standard dust-to-gas ratio value. If in fact this ratio is two orders of magnitude lower for AGN (Maiolino et al. 2001b), marginally obscured AGN (with $N_H \sim 10^{22} \text{ cm}^{-2}$) will be significantly brighter in the optical. For example, a source with $L_X = 10^{43} \text{ ergs s}^{-1}$ and $N_H = 10^{22} \text{ cm}^{-2}$ at $z = 1$ will be ~ 1 magnitude brighter in the z -band if the dust-to-gas ratio is two orders of magnitude smaller than in the Milky Way. For more luminous sources this effect is larger, reaching ~ 5 magnitudes in the z -band for a source with $L_X = 10^{45} \text{ ergs s}^{-1}$ and $N_H = 10^{22} \text{ cm}^{-2}$ at $z = 1$. However, this is about the maximum discrepancy for the sample studied in this paper, since sources with column densities larger than $\sim 5 \times 10^{22} \text{ cm}^{-2}$ or lower than 10^{21} cm^{-2} are not significantly affected in the optical bands since they are already too obscured (and thus dominated by the host galaxy) or the obscuration is too low to make a significant change. Also, the infrared bands are not greatly affected by a change in the dust-to-gas ratio assumed. Therefore, our conclusions

should not be greatly affected by a different choice of dust-to-gas ratio.

Given the small GOODS volume, the contribution of very high redshift sources ($z > 5$) to the total sample is negligible. For these sources, z -band observations ($\lambda_{\text{eff}} \sim 8800 \text{ \AA}$) effectively correspond to $\lambda > 1460 \text{ \AA}$ in the rest frame, and therefore absorption from the intergalactic medium (Madau 1995) can safely be ignored in the whole sample.

To the AGN spectrum we add optical light from a host galaxy, for which we assume an L_* elliptical with spectrum given by Fioc & Rocca-Volmerange (1997). In order to account for the evolution of the host galaxy, caused mainly by star formation, we adopt the evolutionary correction of Poggianti (1997), assuming an elliptical galaxy with an e-folding time of the star formation rate of 1 Gyr. This model predicts an increase in the z -band luminosity of ~ 1.2 magnitudes at redshift ~ 1 . Preliminary results using GOODS optical data (Simmons et al 2004, in prep) show that a large fraction of the AGN host galaxies in the survey are luminous elliptical, justifying our assumption. The host galaxy dominates the optical light for obscured sources with $N_H > 10^{22} \text{ cm}^{-2}$. As an example, for a source with intrinsic hard X-ray luminosity $L_X = 10^{43} \text{ ergs s}^{-1}$ and $N_H = 10^{22} \text{ cm}^{-2}$ the AGN contribution to the total optical light is only $\sim 4\%$ at $z = 0$.

2.2.3. Infrared Spectrum

Optical, UV, and soft X-ray light absorbed by dust within the AGN is re-radiated as thermal emission in the far infrared. Instead of using observed infrared spectra we use the dust-re-emission models of Nenkova et al. (2002); Elitzur et al. (2003) in order to construct a grid of infrared spectra as a function of the X-ray luminosity of the AGN and observed N_H value (related to the line-of-sight angle in these physically-motivated models). These models provide a better fit for recent infrared observations, as well as other advantages over older torus models (e.g. Pier & Krolik 1992, 1993; Granato & Danese 1994); for a detailed discussion of this point see Elitzur et al. (2003).

The Nenkova et al. (2002) models postulate a random distribution of clumps inside a dusty torus. Each clump is optically thick, and the radial distribution is confined between an inner radius R_i and an outer radius R_o (see Figure 2 of Elitzur et al. 2003). The mean free path between clumps is given by a power law of the form r^q where r is the radial distance from the central engine, while the angular dependence of the number of clumps is a Gaussian distribution with dispersion σ , so that the number of clouds as a function of viewing angle β is given by

$$N_T(\beta) = N_T(0) \exp\left(-\frac{\beta^2}{\sigma^2}\right), \quad (4)$$

where β is measured with respect to the equatorial plane. In this work we assume $N_T(0) = 10$, $\sigma = 29^\circ$ and an optical depth of each clump of $\tau_V = 100$, which gives an optical depth at the equator of 1000 (or $N_H = 1.2 \times 10^{24} \text{ cm}^{-2}$ assuming the standard dust to gas ratio) and 0.06 at the poles. This permits AGN ranging from those that are Compton thick down to those that are completely unobscured (although to compare to observations, we assume a minimum column density of $N_H \sim 10^{20} \text{ cm}^{-2}$ for unobscured sources, corresponding to the observed column density through our own Galaxy in the direction of the GOODS-S or GOODS-N fields). Also, we consider three different combinations of values for the parameters R_i/R_o and q ; namely $R_i/R_o = 30$ and $q = 1$, $R_i/R_o = 30$ and $q = 2$ and $R_i/R_o = 100$ and $q = 1$ (Elitzur et al. 2003). All three combinations of values for the parameters generate IR spectra that are consistent with the observations of some local AGN, as can be seen in Figure 2 and in Nenkova et al. (2002). This dust emission model gives an IR spectrum for a given intrinsic N_H .

We calculate the N_H distribution expected from a simple obscuring torus model with fixed geometry and dust distribution and we use this model to convert N_H into viewing angle. From this model we obtain a new N_H function, based on the AGN unification paradigm, called model B in what follows (in contrast to model A, which uses the observed N_H distribution). We assume the torus lies at a distance R_m from the central engine and has height R_t , and that its density distribution is given by

$$\rho(\theta) \propto \exp(-\gamma|\cos \theta|) , \quad (5)$$

(no radial dependence). A schematic diagram of this geometry is shown in Figure 4 and the optical depth as a function of viewing angle is

$$\frac{\tau(\theta)}{\tau_e} = \exp(-\gamma|\cos \theta|) \cos(90 - \theta) \sqrt{\left(\frac{R_m}{R_t}\right)^2 - \sec^2(90 - \theta) \left(\left(\frac{R_m}{R_t}\right)^2 - 1\right)} , \quad (6)$$

where τ_e is the optical depth of the torus at the equatorial plane and γ parameterizes the exponential decay of density with viewing angle. Using a standard dust-to-gas ratio, we can relate optical depth to column density via $N_H = 1.2 \times 10^{21} \tau \text{ cm}^{-2}$ (Bohlin et al. 1978). Then for an equatorial column density $N_H = 10^{24} \text{ cm}^{-2}$, a ratio of radius $R_m/R_t = 1.01$, $\gamma = 4$, and a random distribution of viewing angles, we obtain the model N_H distribution shown in Figure 3.

This set of parameters was selected in order to obtain a ratio of obscured to unobscured of ~ 3 , consistent with the locally observed value (Risaliti, Maiolino, & Salvati 1999) and roughly consistent with population synthesis models that explain the spectrum of the X-ray background. A larger torus at larger radius could also give a 3:1 ratio and would have a cooler

far-infrared spectrum, but until we get the *Spitzer* infrared data, we cannot constrain the far-infrared emission. This distribution is very similar to that observed in the GOODS fields (solid line in Figure 3), except for $N_H > 10^{23} \text{ cm}^{-2}$ sources. For such high column densities, the discrepancy, of the order of 10-15% in the fractional distribution, is probably caused by incompleteness in the *Chandra* samples, since the amount of obscuration is large enough to hide even the hard X-ray emission. In particular, for $N_H \simeq 3 \times 10^{23} \text{ cm}^{-2}$ the incompleteness of the *Chandra* observations in the *Chandra* Deep Fields is $\sim 25\%$, increasing to $\sim 70\%$ for $N_H > 10^{24} \text{ cm}^{-2}$, using the U03 luminosity function and calculating the number of sources below the X-ray flux limit as a function of N_H . Overall, for our model, roughly 50% of the AGN are not detected in the *Chandra* Deep Fields (see § 4.3 for details).

Model B thus comprises the U03 luminosity function (including its redshift evolution), the AGN SEDs described in section §2.2, and the N_H function given by equation 6. Implicit in this model is that the ratio of obscured to unobscured AGN is constant with redshift, and that the geometry of the torus does not change with redshift or luminosity.

For a given luminosity, spectra for different orientation angles are normalized at $100 \mu\text{m}$, where the optical depth is low and thus the re-processed emission from the torus is roughly isotropic. The infrared spectrum is then joined smoothly to the optical spectrum at $1 \mu\text{m}$ so that the resulting spectrum is continuous. Infrared emission from star formation is not considered in this model.

3. Observed and Predicted AGN Number Counts

3.1. The GOODS Data

We compare the number counts calculated above to the optical and X-ray flux distributions for AGN in the two GOODS fields, based on *Chandra* and HST ACS multi-band data. The two GOODS fields, each $10' \times 16'$, were imaged with ACS in the B, V, i and z bands, for a total of 13 orbits per pointing, reaching AB magnitude 27.4 (5σ) in the z band². The GOODS fields have also been imaged extensively from the ground in UBVRIzJHK, and spectroscopy is ongoing. Details of these observations can be found in Giavalisco et al. (2004) and at <http://www.stsci.edu/science/goods>.

GOODS-N and GOODS-S fields have published deep X-ray observations: the 2 Ms

²Observations taken with the NASA/ESA *Hubble Space Telescope (HST)*, which is operated by the Association of Universities for Research in Astronomy, Inc., under NASA contract NAS5-26555.

Chandra Deep Field-North (A03) and the 1 Ms *Chandra* Deep Field-South (Giacconi et al. 2002, hereafter G02). These two ultra-deep X-ray surveys provide the deepest views of the Universe in the 0.5–8.0 keV band. The CDF-N is ≈ 2 times more sensitive at the aim point than the CDF-S, with 0.5–2.0 keV and 2–8 keV flux limits (S/N= 3) of $\approx 2.5 \times 10^{-17}$ erg cm $^{-2}$ s $^{-1}$ and $\approx 1.4 \times 10^{-16}$ erg cm $^{-2}$ s $^{-1}$, respectively (A03). The CDF-N remains $\gtrsim 1.8$ times and $\gtrsim 1.5$ times deeper than the CDF-S over $\approx 50\%$ (≈ 90 arcmin 2) and $\approx 75\%$ (≈ 135 arcmin 2) of the area of GOODS fields, respectively. Point-source *Chandra* catalogs have been produced by A03 for the CDF-N and CDF-S and by G02 for the CDF-S. In this study we use the *Chandra* catalogs of A03 which were generated using the same methods for both fields. These catalogs include 326 sources detected in the CDF-S and 503 in the CDF-N. 223 of the X-ray sources in the CDF-S are located in the GOODS-S region, while 324 of the sources in the CDF-N were found in the GOODS-N region. If only the sources detected in the hard band are included, the sample is reduced to 141 sources in the GOODS-S field and 210 sources in the GOODS-N region.

The GOODS fields will be observed with the *Spitzer* IRAC instrument in all four bands (3.6 to 8 μ m), with expected sensitivity of 0.6 μ Jy in the 3.6 μ m band. Both fields will also be observed with the *Spitzer* MIPS instrument at 24 microns, to a flux limit that depends somewhat on the as-yet unknown source density (and hence confusion limit), but which we take to be roughly 22 μ Jy (5σ).

There are 168 published spectroscopic redshifts for X-ray sources in the CDF-S, all of them measured using the FORS1 and FORS2 cameras at the VLT telescopes (Szokoly et al. 2004). Photometric redshifts have been calculated for all the sources detected in the optical bands in the GOODS South field (see Mobasher et al. 2004 for details), which account for $\sim 90\%$ of the observed X-ray sources. Properties of some of the remaining sources not detected in the ACS observations are described in detail by Koekemoer et al. (2004). Spectroscopic redshifts were used when available.

Spectroscopic redshifts for 284 X-ray sources in the CDF-N were obtained by Barger et al. (2003) using the Low-Resolution Imaging Spectrograph and the Deep Extragalactic Imaging Multi-Object Spectrograph on the Keck 10-m telescopes and the HYDRA spectrograph on the WIYN 3.5-m telescope. Photometric redshifts were used when spectroscopic redshifts were not available (see Barger et al. 2003). Spectroscopic redshifts were obtained for 54% of the sources, while if photometric redshifts are added the completeness level rises to $\sim 75\%$. Sources without spectroscopic or photometric redshifts are very faint in the optical, with all but two having $z > 24.0$ mag. Given the very faint magnitudes of the sources without redshifts in the GOODS-N region, they are likely at redshift $z > 1.0$ and lack the strong broad emission lines normally used to identify unobscured AGN at high redshift. That is,

most are probably obscured AGN at $z > 1$ (e.g., Alexander et al. 2001; Koekemoer et al. 2002).

3.2. The AGN Sample

Almost all the X-ray sources detected in the GOODS fields are AGN, with the exception of a few nearby starburst galaxies (Alexander et al. 2003). Sources in the X-ray catalogs were matched to the ACS images of the GOODS North and South fields by Bauer et al. (2004, in prep) using the likelihood method described in Bauer et al. (2000). Using only X-ray sources that were detected in the hard band and were unambiguously identified in the optical images (i.e., only one optical counterpart within ~ 1 arcsecond of the X-ray centroid), the final sample includes 128 sources in the GOODS South region and 178 in the GOODS North field. It is important to note that reducing the analysis to the unambiguously matched sources eliminates $\sim 10\%$ of the hard X-ray sources in the GOODS regions. Roughly half of these sources in the GOODS-S field have counterparts in deep K -band imaging and thus may be obscured AGN at high redshift (Koekemoer et al. 2004). Optically faint X-ray sources detected in near-infrared bands in other fields were also discussed by Mainieri et al. (2002) and Mignoli et al. (2004).

3.3. Deriving the N_H Distribution from the *Chandra* Data

The hardness ratio, which we calculate for each source, is defined as $(H - S)/(H + S)$, where S is the number of counts detected in the 0.5 – 2 keV band and H is the number of counts in the 2 – 8 keV band. The neutral hydrogen column density was calculated from the hardness ratio assuming an intrinsic power-law X-ray spectrum with photon indices $\Gamma = 1.7$ or $\Gamma = 1.9$. We generated a conversion table using XSPEC (Arnaud 1996) to calculate hardness ratios for a range of N_H and redshift values; this program incorporates the *Chandra* ACIS instrumental response matrix. We added Galactic absorption column densities (Stark et al. 1992) at $z = 0$ of $N_H = 8 \times 10^{19} \text{ cm}^{-2}$ for the GOODS-S field and $N_H = 1.6 \times 10^{20} \text{ cm}^{-2}$ in the GOODS-N field to each N_H - z pair stored in the table, since all X-rays pass through the interstellar medium of our galaxy. Using the table, the hardness ratio of each source with a spectroscopic redshift (photometric redshifts are too uncertain for this purpose) can be converted to a value of N_H . The distribution of derived N_H values for 82 sources with spectroscopic redshifts in the GOODS-S field and 103 sources in the GOODS-N field is shown in Figure 3. Note that for individual sources, our method of deriving N_H may not be very accurate, as some will have soft excess emission or intrinsically

soft spectra (indeed, these may be the reasons why there is an excess of apparently low column density objects) or will have intrinsically steeper spectra (and thus have spuriously high N_H) and therefore our resulting distribution can be affected by systematic errors. In order to minimize these effects, the value of N_H determined for each source is only used to calculate the distribution of the sample and not for other purposes (e.g. to correct the observed X-ray flux).

The predicted N_H distributions for the sources in the GOODS N+S fields in models A and B are compared in Figure 3. Model B provides a better fit to the observed data; a K-S test on both models compared to the observations revealed that the null hypothesis (that the model and observed distributions are drawn from the same parent distribution) is acceptable at the 75.3% confidence level for model B and at the 58.5% confidence level for model A. This is not surprising since model B uses an N_H function with parameters chosen to be consistent with the observations; however, it is important to note that this model is motivated by the unification paradigm, which clearly can account for the observed N_H distribution.

3.4. X-ray Number Counts

The total area covered as a function of X-ray flux limit for each GOODS field was calculated based on the results presented in A03 and is shown in Figure 5. These curves are needed to normalize the hard X-ray flux distributions for sources in the GOODS fields, shown in Figure 6. We also plot the X-ray distributions calculated from the hard X-ray luminosity function U03 for both models A (U03 observed N_H function) and B (our N_H function based on a simple unified model). The agreement is very good for both models; a K-S test shows that the null hypothesis is acceptable at $> 90\%$ confidence when either model was tested against the observed distribution. Although the U03 sample includes the CDF-N, this is not a circular argument since in that work only the brightest CDF-N sources (with $f_X > 3 \times 10^{-15}$ ergs cm $^{-2}$ s $^{-1}$ in the hard band) were considered, and therefore our calculation tests the extrapolation to much fainter fluxes. In the hard X-ray flux distribution both unobscured (type 1) and obscured (type 2) AGN are well represented (dotted and dashed lines in Figure 6).

3.5. Optical Number Counts

In deep optical imaging with the HST ACS camera the vast majority of the X-ray sources in the GOODS fields are detected. Figure 7 shows the distribution of observed z -band magnitudes for the X-ray sources in the two fields combined (solid line), along with the model predictions (dashed line). The agreement between the observed and predicted distributions is very good; a K-S test comparing the observed distribution to the prediction of model B gives a confidence level for the null hypothesis of 71%, while for model A the confidence level is 53%. The observed distribution is very broad, with the brightest objects at $z \sim 17$ mag and the faintest below $z \sim 28$ mag. Unobscured AGN (dashed line) fail to account for the faintest optical counterparts. Given their large X-ray to optical flux ratios, the fainter optical sources ($z > 23.5$ mag) may be obscured AGN at redshifts $z \sim 1 - 3$ (Alexander et al. 2001; Koekemoer et al. 2002). Indeed in our models most obscured AGN (dotted line) have faint optical magnitudes, while the unobscured AGN are responsible for the peak at brighter magnitudes. For $z > 23.5$ mag, the approximate limit for ground-based spectroscopy, obscured AGN are the dominant population.

3.6. Redshift Distribution

Figure 8 shows the redshift distributions for the sources in the GOODS-North and South fields (thick solid lines) compared to the expected redshift distributions from our model B (dashed lines). Using photometric redshifts (Mobasher et al. 2004), our GOODS-S sample of hard X-ray sources is 100% complete. However, in the GOODS-N field, combining spectroscopic and photometric redshifts (Barger et al. 2003), the sample is only $\sim 75\%$ complete³. Spectroscopic redshifts are shown by the hatched regions. At redshifts above $z \sim 1$, there is a clear discrepancy between the spectroscopic redshifts and either the photometric redshift or the model predictions, in the sense that there are fewer AGN with high spectroscopic redshifts. This is explained at least in part by the effective brightness limit for spectroscopy, $R < 24$ mag, for even the largest ground-based telescopes. Imposing this optical limit on the GOODS AGN model (long dashed line in Figure 8) does match the observed spectroscopic redshift distribution very well. Obscured AGN at $z > 1$, in particular, are fainter than this limit and thus are not included in the spectroscopic samples. This likely accounts for the discrepancy between the observed redshift distribution of X-ray sources (Hasinger 2002; Szokoly et al. 2004) and the distribution predicted from population synthesis models for the X-ray background (Gilli et al. 1999, 2001), as well as the low number of Type 2 AGN

³We expect the photometric redshifts to be 100% complete once the GOODS ACS data are fully analyzed.

identifications.

The agreement between the model and the observations is good, with a K-S test giving 63% confidence for the null hypothesis in the GOODS-S field and 21% confidence in the GOODS-N field. This slightly lower level arises because the model predicts still more high redshift AGN than are observed in the GOODS fields. This is because some high-redshift obscured AGN are too faint even for the HST images (see Koekemoer et al. 2004) and because the most obscured AGN are not detected in the *Chandra* deep fields. Also, an excess of observed sources at $z < 1$ can be seen. This is explained by the presence of clusters and large scale structure in both fields (e.g. Gilli et al. 2003).

Figure 8 shows the difference between the North and South fields, in the sense that there is a larger discrepancy between the photometric redshifts and the model in the North. This must be due to incompleteness since again the missing 25% of the AGN (those without photometric or spectroscopic redshifts) are preferentially fainter.

The model redshift distribution is therefore in agreement with the data once these selection effects are considered. It is also compatible with the kind of distribution predicted from population synthesis (Gilli et al. 2001), in the sense that it peaks at a higher redshift than previously reported distributions, with the same caveat about selection effects. This better agreement between models and observations is explained also in part by the use of the U03 luminosity function, that includes a redshift distribution that peaks at lower redshifts than existing optical quasar luminosity functions (e.g. Boyle et al. 2000).

4. Discussion

Hard X-ray surveys find obscured sources that are largely missed in deep optical/UV surveys. Deriving a hard X-ray luminosity function or a redshift distribution imposes an effective optical cut at $R < 24$ mag, since optical spectroscopy is required to obtain redshifts. Thus published redshift distributions can be missing optically faint sources. These sources can be either low-luminosity unobscured AGN or obscured AGN, depending on their central engine luminosity, and in general, the spectroscopic incompleteness increases with redshift. This selection effect explains the discrepancy between the photometric and spectroscopic redshift distributions (Fig. 8).

Evidence for the existence of a significant number of obscured AGN at $z > 1$ was previously given by Fiore et al. (2003), who found a correlation between X-ray luminosity and X-ray-to-optical flux ratio in obscured AGN. Such a correlation can be explained by our models since for obscured AGN the optical light is dominated by the host galaxy, which is

independent of the AGN luminosity. Therefore, for an obscured AGN the optical emission is roughly constant, while the X-ray emission scales directly with the AGN luminosity. Using this correlation, Fiore et al. (2003) estimated source redshifts using just the X-ray-to-optical flux ratio, thus including sources too faint for optical spectroscopy. They concluded there is a significant number of obscured AGN at $z > 1$, and that these sources will be missed by surveys that rely on optical spectroscopy. We arrive at the same conclusion from a different direction, based on the comparison of our model with multiwavelength observations of X-ray sources.

4.1. Optically Faint X-ray Sources

The GOODS HST data reveal an appreciable number of optically faint, X-ray-selected AGN. While unobscured sources are bright in the optical bands, the vast majority of them brighter than the spectroscopic limit, obscured sources will be optically fainter and therefore missed preferentially by surveys that depend on spectroscopic identifications. Most obscured AGN are bright enough in hard X-rays to be detected in the *Chandra* observations. Therefore, given the large X-ray-to-optical flux ratios of the optically faint sample, their hardness ratio and their red colors, they are very likely to be obscured AGN at $z > 1$ (Alexander et al. 2001; Koekemoer et al. 2002). Sources with high X-ray-to-optical flux ratio in other fields were discussed previously in the literature (e.g., Fiore et al. 2003; Mignoli et al. 2004; Gandhi, Crawford, Fabian, & Johnstone 2004), and in most cases these sources can be identified as obscured AGN at high redshift.

4.2. N_H Distribution

Both models for the N_H distribution fit the observed flux distributions well (Figs 6,7). Model A assumed the empirical N_H function described in U03, which is based on observations from several X-ray surveys and did not go as deep as the GOODS sample, while model B uses an N_H function based on a simple unified model, with the idea of a dust torus covering the central engine. It is important to note that model B predicts a larger number of sources with $N_H \sim 10^{23} \text{ cm}^{-2}$ than is observed, commensurate with the large number of very obscured sources needed to explain the X-ray background spectrum (Gilli et al. 2001,U03). The *observed* ratio of obscured to unobscured sources in the GOODS fields is ~ 2.5 when the division point is set at $N_H = 10^{21} \text{ cm}^{-2}$ as assumed by Gilli et al. (2001), less than the intrinsic value of 4 required by the X-ray background models. That is, the observed ratio is affected by incompleteness in the X-ray samples at high column densities. Based on the U03

luminosity function and our torus model to calculate the N_H distribution we calculate that the completeness level of the *Chandra* observations in the GOODS fields drops to $\sim 75\%$ for $N_H = 10^{23} \text{ cm}^{-2}$ and $\sim 30\%$ for $N_H = 10^{24} \text{ cm}^{-2}$. This is caused by absorption of the X-ray emission which makes harder to detect sources with higher column densities in a flux-limited survey. Therefore, if there are heavily obscured AGN in the field, the intrinsic ratio of obscured to unobscured sources is larger than the observed ratio, and can even be ~ 4 , as suggested by population synthesis models for the X-ray background. The relation between the observed X-ray sources in the GOODS fields and the models for the X-ray background will be analyzed in more detail in a later paper (Treister et al. 2004, in prep.).

We can ask whether the X-ray absorption correlates with the optical dimming; that is, is obscuration making bright hard X-ray sources optically faint? The relation between optical magnitude and amount of obscuration is shown in Figure 9. Sources that present large amounts of obscuration in the X-ray spectrum are in general the fainter sources in the optical, as expected. There is no strong correlation present in Figure 9 — both obscured and unobscured AGN appear at bright magnitudes — but the highest column densities do correspond to the faintest magnitudes. In particular, it is important to note that there are no unobscured sources at magnitudes $i > 24.5$, which is consistent with our model predictions of a very low number of unobscured AGN at faint magnitudes. There is no strong correlation because the optical emission from obscured AGN is dominated by the host galaxy; once the optical emission of the AGN is absorbed, the i -band magnitude becomes insensitive to the amount of obscuration or to the intrinsic luminosity of the AGN.

The full X-ray (0.5-8 keV) to optical (z -band) flux ratio⁴ for GOODS AGN is shown in Figure 10, together with the ratio obtained from our model. The agreement between these two distributions is very good, with a K-S confidence level of $\sim 92\%$ for the null hypothesis, except for a small discrepancy at $\log F_X/F_{\text{opt}} > 0.5$, which is consistent with the previously calculated incompleteness of the X-ray samples for $N_H > 10^{23} \text{ cm}^{-2}$. A second discrepancy appears at the low F_X/F_{opt} end, which can be explained by the presence of a few starburst galaxy and other non-AGN X-ray sources in the *Chandra* Deep Fields observations (e.g., Hornschemeier et al. 2001; Alexander et al. 2002; Bauer et al. 2002). These sources, around 10% of the total sample, are not accounted in our model and therefore increase the number of observed X-ray sources with $\log F_X/F_{\text{opt}} < -2$. This number of non-AGN X-ray sources is in agreement with the values reported by A03.

⁴Defined as $\log F_X/F_{\text{opt}} = \log F_X + 0.4 \times m_z + 4.934$, where F_X is the X-ray flux in units of $\text{ergs cm}^{-2} \text{ s}^{-1}$ and m_z is the optical magnitude in the z band in the AB system.

4.3. Predictions for the Infrared Number Counts

The *Spitzer* Space Telescope was launched in August 2003 and the GOODS fields are scheduled to be observed in 2004. AGN are luminous infrared sources (Sanders et al. 1989), so the ratio of obscured to unobscured AGN will be strongly constrained by the observed *Spitzer* number counts of X-ray sources. These two classes can be separated using a combination of IRAC 4.5 and 8 microns bands and MIPS 24 microns data (Andreani et al. 2003). Furthermore, the infrared spectrum is sensitive to parameters of the dust emission model, so will help refine the present simple spectral models.

The AGN number counts at 24 μm calculated according to § 2 assuming the appropriate hard X-ray flux limit for each *Chandra* deep field separately, and normalized to the total GOODS area (0.08 deg²), are shown in Figure 11; the number counts at 8 μm and 3.6 μm are presented in Figures 12 and 13. Contributions from obscured and unobscured AGN were calculated from hard X-ray luminosity functions using model B. For the infrared part of the SED, we assumed three different sets of parameters, as is described in §2.2; each shaded region for the total and obscured number of sources corresponds to the extremes that these values can have. For unobscured sources, the shape of the infrared SED is almost independent of the assumed parameters, so only one line is plotted.

One important conclusion from this calculation is that all the AGN detected in the *Chandra* deep fields should be detected in the *Spitzer* observations. The contrary is not the case since some obscured AGN are missed by X-ray observations. This difference is shown by the top two curves in Figure 11. Indeed, obscured AGN with $N_H > 10^{23} \text{ cm}^{-2}$ should all be detected with *Spitzer*, in principle allowing for a complete study of the AGN population in this field and providing a test for both the unified model of AGN and the population synthesis models used to explain the X-ray background. However, to identify obscured AGN not detected in X-rays and to separate them from luminous starburst galaxies will not be easy. In fact, Andreani et al. (2003) reported that is not possible to separate very obscured AGN activity from a burst of star formation just on the basis of infrared photometry, even if information in the MIPS 70-micron band is included. This problem is even more serious since typically there is overlap between the two populations, and a starburst galaxy can harbor a very obscured AGN. In order to solve this problem, we can take advantage of GOODS multiwavelength coverage, ranging from 0.4 to 24 microns, which allows us to calculate accurate photometric redshifts and bolometric luminosities for even very faint sources. Then, to first order, we can use bolometric luminosity in order to separate AGN activity from starburst galaxies, since all AGN should have $L_{\text{bol}} > 10^{42} \text{ ergs s}^{-1}$, while starbursts typically have much lower luminosities.

Similar calculations of the AGN number counts in the infrared were performed recently

by Andreani et al. (2003). For $\Omega_\Lambda = 0.7$ and $\Omega_m = 0.3$, they found a total of $\sim 3 \times 10^5$ sources per square degree with a 24 μm flux higher than 550 μJy , $\sim 10\%$ of them Seyfert 2s. We predict a much lower number of sources, $\sim 10^3$ sources per square degree at the same flux limit in the 24 μm band, with $\sim 70\%$ of them being Seyfert 2s. This large discrepancy of 2 orders of magnitude can be explained by the difference in the assumed luminosity function and evolution. We used a hard X-ray luminosity function and luminosity-dependent density evolution, which peaks at redshifts $z \sim 2$ for QSO-like objects and $z \lesssim 1$ for low-luminosity AGN, whereas Andreani et al. (2003) used a local luminosity function based on 12- μm observations and optical QSO evolution with a peak at $z \sim 3$ and exponential decay until $z = 10$. Locally both luminosity functions are very similar so the major part of the discrepancy is explained by the difference in the assumed evolution. This shows clearly that *Spitzer* observations will provide a significant constraint on the AGN number density evolution.

5. Conclusions

In this work we modeled the AGN population of the GOODS fields in order to explain the observed numbers and brightnesses at optical and X-ray energies. We also predicted the number counts at infrared wavelengths that will be measured with the *Spitzer* Space Telescope. Basic ingredients of our models are few. First, we used the hard X-ray luminosity function and luminosity-dependent evolution determined by U03. Second, we developed a library of multi-wavelength AGN SEDs parameterized as a function of only two parameters, the intrinsic rest-frame hard X-ray luminosity and the amount of gas and dust in the line of sight, given as a neutral hydrogen column density. These composite SEDs assume an intrinsic power law plus photoelectric absorption in X-rays; a QSO composite spectrum in the optical, independent of both redshift and luminosity; Milky Way-type extinction; an L_* elliptical host galaxy evolving with redshift; and infrared dust re-emission models from Nenkova et al. (2002) and Elitzur et al. (2003). Finally, we needed to assume the relative number of sources at each value of N_H . In model A, we used the N_H function given in U03, which is based on observations of X-ray sources in several surveys. For model B, we used a simple geometric model for a dust torus to generate the expected distribution of N_H for random orientation angles. The torus parameters were chosen so that the ratio of obscured ($N_H > 10^{22} \text{ cm}^{-2}$) to unobscured AGN is 3:1, and we assumed it was independent of redshift and luminosity. With these ingredients, we calculated the expected distribution of sources at different wavebands and compared them to the GOODS observations.

We found general agreement between the models and observations, especially for the very

simple unified model. This means there may well be a significant population of obscured AGN at high redshift, consistent with a roughly constant ratio of obscured to unobscured AGN out to high redshift, $z \sim 2 - 3$. These objects will be bright enough to detect with the planned *Spitzer* observations in the GOODS field. The agreement between model and observations is remarkable given the very simple assumptions used in the calculation. Because the GOODS observations are so deep, there are large extrapolations from existing luminosity functions. The excellent agreement supports the unified model of AGN.

A large population of obscured AGN in the early Universe explains not only the GOODS data but the X-ray background spectral shape and intensity. However, for this picture to be correct, existing X-ray samples, even from the extremely deep *Chandra* fields, must be incomplete. We find that the luminosity-function-weighted fraction of obscured AGN that is missed at current detection limits is approximately equal to the excess predicted by our unified model at faint optical magnitudes and high absorbing column densities. *Spitzer* observations, together with follow-up studies of host galaxy morphologies and environments, offer the opportunity to test and refine this picture.

ET thanks the support of Fundacion Andes. This work was supported in part by NASA grant HST-GO-09425.13-A. The work of DS was carried out at Jet Propulsion Laboratory, California Institute of Technology, under a contract with NASA. We thank the anonymous referee for a very detailed and useful report. We would like to thank Eric Gawiser, Priya Natarajan, Paolo Coppi and Paulina Lira for very useful comments. We thank Moshe Elitzur for providing us a digital version of his infrared dust re-emission models.

REFERENCES

- Akiyama, M., Ueda, Y., Ohta, K., Takahashi, T., & Yamada, T. 2003, *ApJS*, 148, 275
- Alexander, D. M., Aussel, H., Bauer, F. E., Brandt, W. N., Hornschemeier, A. E., Vignali, C., Garmire, G. P., & Schneider, D. P. 2002, *ApJ*, 568, L85
- Alexander, D. M., Bauer, F. E., Brandt, W. N., Schneider, D. P., Hornschemeier, A. E., Vignali, C., Barger, A. J., Broos, P. S., Cowie, L. L., Garmire, G. P., Townsley, L. K., Bautz, M. W., Chartas, G., & Sargent, W. L. W. 2003, *AJ*, 126, 539
- Alexander, D. M., Brandt, W. N., Hornschemeier, A. E., Garmire, G. P., Schneider, D. P., Bauer, F. E., & Griffiths, R. E. 2001, *AJ*, 122, 2156
- Andreani, P., Spinoglio, L., & Malkan, M. A. 2003, *ApJ*, 597, 759

- Antonucci, R. 1993, *ARA&A*, 31, 473
- Arnaud, K. A. 1996, in *ASP Conf. Ser. 101: Astronomical Data Analysis Software and Systems V*, 17–+
- Barcons, X., Franceschini, A., de Zotti, G., Danese, L., & Miyaji, T. 1995, *ApJ*, 455, 480
- Baldi, A., Molendi, S., Comastri, A., Fiore, F., Matt, G., & Vignali, C. 2002, *ApJ*, 564, 190
- Barger, A. J., Cowie, L. L., Capak, P., Alexander, D. M., Bauer, F. E., Fernandez, E., Brandt, W. N., Garmire, G. P., & Hornschemeier, A. E. 2003, *AJ*, 126, 632
- Bassani, L., Dadina, M., Maiolino, R., Salvati, M., Risaliti, G., della Ceca, R., Matt, G., & Zamorani, G. 1999, *ApJS*, 121, 473
- Bauer, F. E., Alexander, D. M., Brandt, W. N., Hornschemeier, A. E., Miyaji, T., Garmire, G. P., Schneider, D. P., Bautz, M. W., Chartas, G., Griffiths, R. E., & Sargent, W. L. W. 2002, *AJ*, 123, 1163
- Bauer, F. E., Condon, J. J., Thuan, T. X., & Broderick, J. J. 2000, *ApJS*, 129, 547
- Bohlin, R. C., Savage, B. D., & Drake, J. F. 1978, *ApJ*, 224, 132
- Boyle, B. J., Shanks, T., Croom, S. M., Smith, R. J., Miller, L., Loaring, N., & Heymans, C. 2000, *MNRAS*, 317, 1014
- Brandt, W. N., Alexander, D. M., Hornschemeier, A. E., Garmire, G. P., Schneider, D. P., Barger, A. J., Bauer, F. E., Broos, P. S., Cowie, L. L., Townsley, L. K., Burrows, D. N., Chartas, G., Feigelson, E. D., Griffiths, R. E., Nousek, J. A., & Sargent, W. L. W. 2001, *AJ*, 122, 2810
- Cardelli, J. A., Clayton, G. C., & Mathis, J. S. 1989, *ApJ*, 345, 245
- Castander, F. J., Treister, E., Maza, J., Coppi, P. S., Maccarone, T. J., Zepf, S. E., Guzmán, R., & Ruiz, M. T. 2003, *Astronomische Nachrichten*, 324, 40
- Comastri, A., Setti, G., Zamorani, G. & Hasinger, G. 1995, *A&A*, 296, 1
- Dawson, S., McCrady, N., Stern, D., Eckart, M. E., Spinrad, H., Liu, M. C., & Graham, J. R. 2003, *AJ*, 125, 1236
- Dickinson, M. & Giavalisco, M. 2002, in *The Mass of Galaxies at Low and High Redshift*, in press, astro-ph/0204213

- Elitzur, M., Nenkova, M., & Ivezić, Z. 2003, astro-ph/0309040
- Elvis, M., et al. 1994, ApJS, 95, 1
- Fioc, M. & Rocca-Volmerange, B. 1997, A&A, 326, 950
- Fiore, F., et al. 2003, A&A, 409, 79
- Gandhi, P., Crawford, C. S., Fabian, A. C., & Johnstone, R. M. 2004, MNRAS, 348, 529
- Giacconi, R., Rosati, P., Tozzi, P., Nonino, M., Hasinger, G., Norman, C., Bergeron, J., Borgani, S., Gilli, R., Gilmozzi, R., & Zheng, W. 2001, ApJ, 551, 624
- Giacconi, R., Zirm, A., Wang, J., Rosati, P., Nonino, M., Tozzi, P., Gilli, R., Mainieri, V., Hasinger, G., Kewley, L., Bergeron, J., Borgani, S., Gilmozzi, R., Grogan, N., Koekemoer, A., Schreier, E., Zheng, W., & Norman, C. 2002, ApJS, 139, 369
- Giavalisco, M. et al. 2004, ApJ, 600, L93
- Gilli, R., Risaliti, G., & Salvati, M. 1999, A&A, 347, 424
- Gilli, R., Salvati, M., & Hasinger, G. 2001, A&A, 366, 407
- Gilli, R. 2003, Adv. Space Res., in press(astro-ph/0303115)
- Gilli, R., et al. 2003, ApJ, 592, 721
- Granato, G. L. & Danese, L. 1994, MNRAS, 268, 235
- Green, P. J., et al. 2004, ApJS, 150, 43
- Gruber, D. E. 1992, in The X-ray Background, 44
- Harrison, F. A., Eckart, M. E., Mao, P. H., Helfand, D. J., & Stern, D. 2003, ApJ, 596, 944
- Hasinger, G. 2002, in New Visions of the X-ray Universe in the XMM-Newton and Chandra Era, Ed. F. Jansen (ESTEC: ESA SP-488), XX (astro-ph/0202430)
- Hornschemeier, A. E., Brandt, W. N., Garmire, G. P., Schneider, D. P., Barger, A. J., Broos, P. S., Cowie, L. L., Townsley, L. K., Bautz, M. W., Burrows, D. N., Chartas, G., Feigelson, E. D., Griffiths, R. E., Lumb, D., Nousek, J. A., Ramsey, L. W., & Sargent, W. L. W. 2001, ApJ, 554, 742

- Koekemoer, A. M., Grogin, N. A., Schreier, E. J., Giacconi, R., Gilli, R., Kewley, L., Norman, C., Zirm, A., Bergeron, J., Rosati, P., Hasinger, G., Tozzi, P., & Marconi, A. 2002, *ApJ*, 567, 657
- Koekemoer, A. M. et al. 2004, *ApJ*, 600, L123
- Lawrence, A. 1987, *PASP*, 99, 309
- Madau, P., Ghisellini, G., & Fabian, A. C. 1994, *MNRAS*, 270, L17
- Madau, P. 1995, *ApJ*, 441, 18
- Mainieri, V., Bergeron, J., Hasinger, G., Lehmann, I., Rosati, P., Schmidt, M., Szokoly, G., & Della Ceca, R. 2002, *A&A*, 393, 425
- Maiolino, R., Marconi, A., & Oliva, E. 2001a, *A&A*, 365, 37
- Maiolino, R., Marconi, A., Salvati, M., Risaliti, G., Severgnini, P., Oliva, E., La Franca, F., & Vanzì, L. 2001b, *A&A*, 365, 28
- Mignoli, M., et al. 2004, *A&A*, 418, 827
- Mobasher, B. et al. 2004, *ApJ*, 600, L167
- Morrison, R. & McCammon, D. 1983, *ApJ*, 270, 119
- Mushotzky, R. F., Boldt, E. A., Holt, S. S., Serlemitsos, P. J., Swank, J. H., Rothschild, R. H., & Pravdo, S. H. 1978, *ApJ*, 226, L65
- Mushotzky, R. F., Done, C., & Pounds, K. A. 1993, *ARA&A*, 31, 717
- Nandra, K. & Pounds, K. A. 1994, *MNRAS*, 268, 405
- Nandra, K., George, I. M., Mushotzky, R. F., Turner, T. J., & Yaqoob, T. 1997, *ApJ*, 476, 70
- Nenkova, M., Ivezić, Ž., & Elitzur, M. 2002, *ApJ*, 570, L9
- Norman, C., Hasinger, G., Giacconi, R., Gilli, R., Kewley, L., Nonino, M., Rosati, P., Szokoly, G., Tozzi, P., Wang, J., Zheng, W., Zirm, A., Bergeron, J., Gilmozzi, R., Grogin, N., Koekemoer, A., & Schreier, E. 2002, *ApJ*, 571, 218
- Perola, G. C. et al., *A&A*, in press, astro-ph/0404044.

- Pier, E. A. & Krolik, J. H. 1992, *ApJ*, 401, 99
- Pier, E. A. & Krolik, J. H. 1993, *ApJ*, 418, 673
- Poggianti, B. M. 1997, *A&AS*, 122, 399
- Risaliti, G., Maiolino, R., & Salvati, M. 1999, *ApJ*, 522, 157
- Rosati, P., Tozzi, P., Giacconi, R., Gilli, R., Hasinger, G., Kewley, L., Mainieri, V., Nonino, M., Norman, C., Szokoly, G., Wang, J. X., Zirm, A., Bergeron, J., Borgani, S., Gilmozzi, R., Grogin, N., Koekemoer, A., Schreier, E., & Zheng, W. 2002, *ApJ*, 566, 667
- Sanders, D. B., Phinney, E. S., Neugebauer, G., Soifer, B. T., & Matthews, K. 1989, *ApJ*, 347, 29
- Setti, G., Woltjer, L. 1989, *A&A*, 224L, 21
- Singh, K. P., Barrett, P., White, N. E., Giommi, P., & Angelini, L. 1995, *ApJ*, 455, 456
- Stark, A. A., Gammie, C. F., Wilson, R. W., Bally, J., Linke, R. A., Heiles, C., & Hurwitz, M. 1992, *ApJS*, 79, 77
- Steffen, A. T., Barger, A. J., Cowie, L. L., Mushotzky, R. F., & Yang, Y. 2003, *ApJ*, 596, L23
- Steidel, C. C., Hunt, M. P., Shapley, A. E., Adelberger, K. L., Pettini, M., Dickinson, M., & Giavalisco, M. 2002, *ApJ*, 576, 653
- Stern, D., Moran, E. C., Coil, A. L., Connolly, A., Davis, M., Dawson, S., Dey, A., Eisenhardt, P., Elston, R., Graham, J. R., Harrison, F., Helfand, D. J., Holden, B., Mao, P., Rosati, P., Spinrad, H., Stanford, S. A., Tozzi, P., & Wu, K. L. 2002, *ApJ*, 568, 71
- Szokoly, G. et al. 2004, *ApJS* in press, astro-ph/0312324
- Ueda, Y., Akiyama, M., Ohta, K., & Miyaji, T. 2003, *ApJ*, 598, 886 (U03)
- Vanden Berk, D. E. et al. 2001, *AJ*, 122, 549
- Vignali, C., Brandt, W. N., & Schneider, D. P. 2003, *AJ*, 125, 433
- Voges, W. et al. 1999, *A&A*, 349, 389
- Weingartner, J. C. & Murray, N. 2002, *ApJ*, 580, 88

Williams, R. E., et al. 1996, AJ, 112, 1335

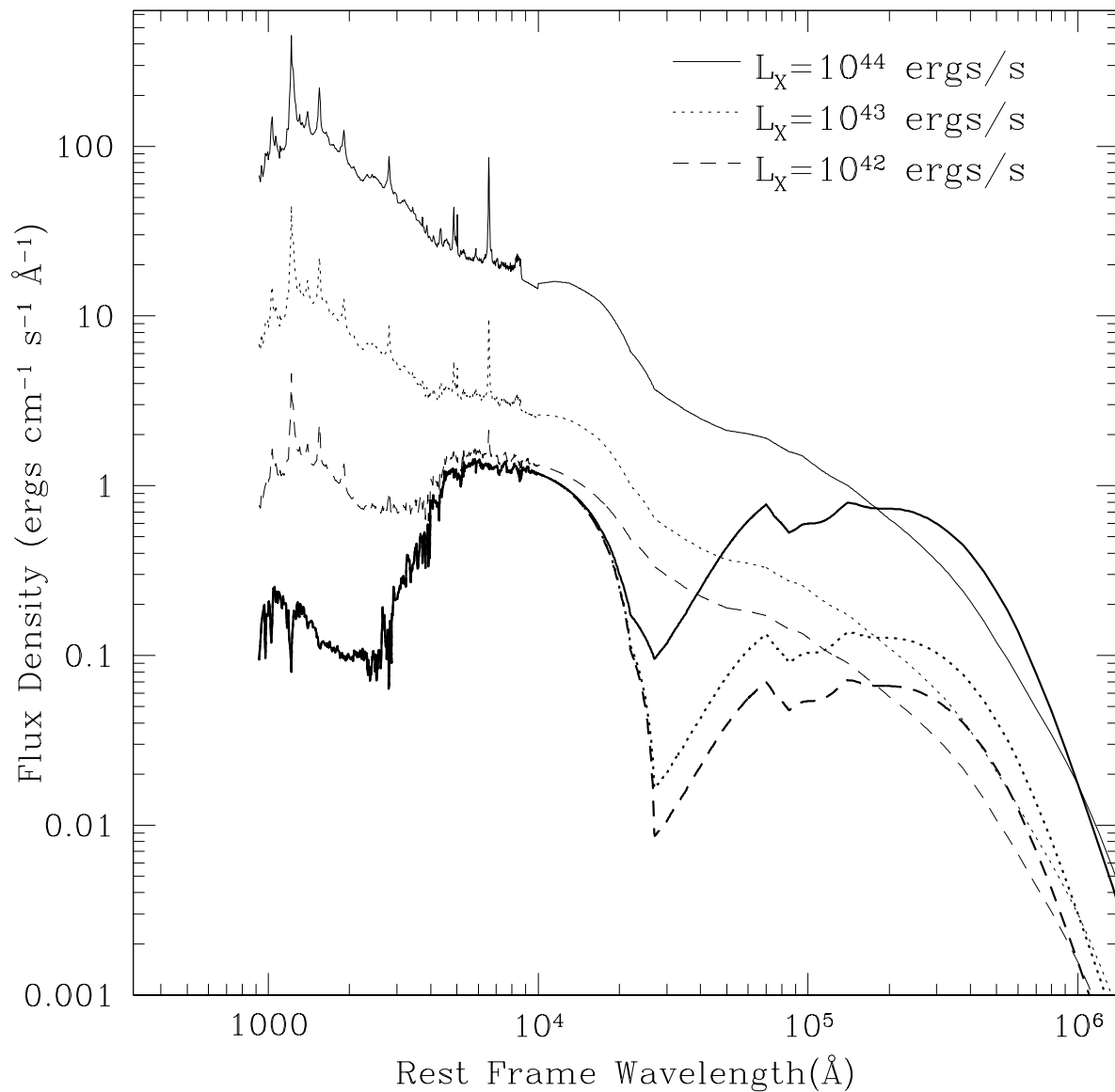


Fig. 1.— UV to far IR spectral energy distributions for AGN with three intrinsic hard X-ray (2-8 keV) luminosities, L_X , and neutral hydrogen column densities, N_H , ranging from 10^{20} cm^{-2} (*light lines*) to 10^{24} cm^{-2} (*heavy lines*). Details about these model SEDs can be found in § 2.1.

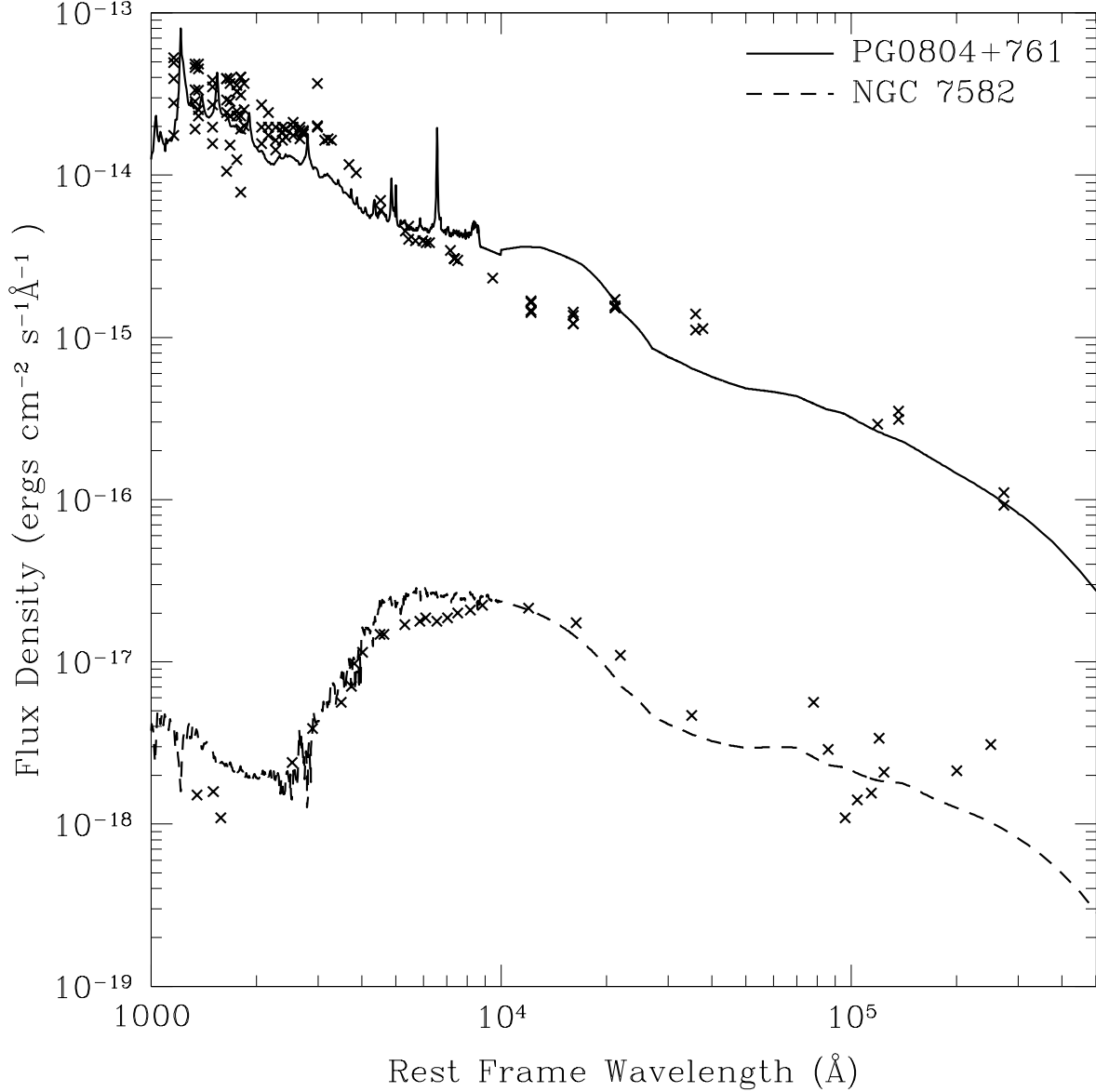


Fig. 2.— Spectral Energy Distributions for the Type 1 quasar PG0804+761 (upper crosses) and the Seyfert 2 galaxy NGC 7582 (lower crosses). Over-plotted are our model SEDs (solid and dashed lines) for the appropriate L_X and N_H ; an X-ray luminosity of $L_X = 8.5 \times 10^{45}$ ergs s⁻¹ and $N_H = 3 \times 10^{20}$ cm⁻² for PG0804+761 (Elvis et al. 1994) and $L_X = 9.4 \times 10^{41}$ ergs s⁻¹ and $N_H = 1.2 \times 10^{23}$ cm⁻² for NGC 7582 (Bassani et al. 1999). With no free parameters to adjust, the agreement between the model SED and the observed values is remarkably good.

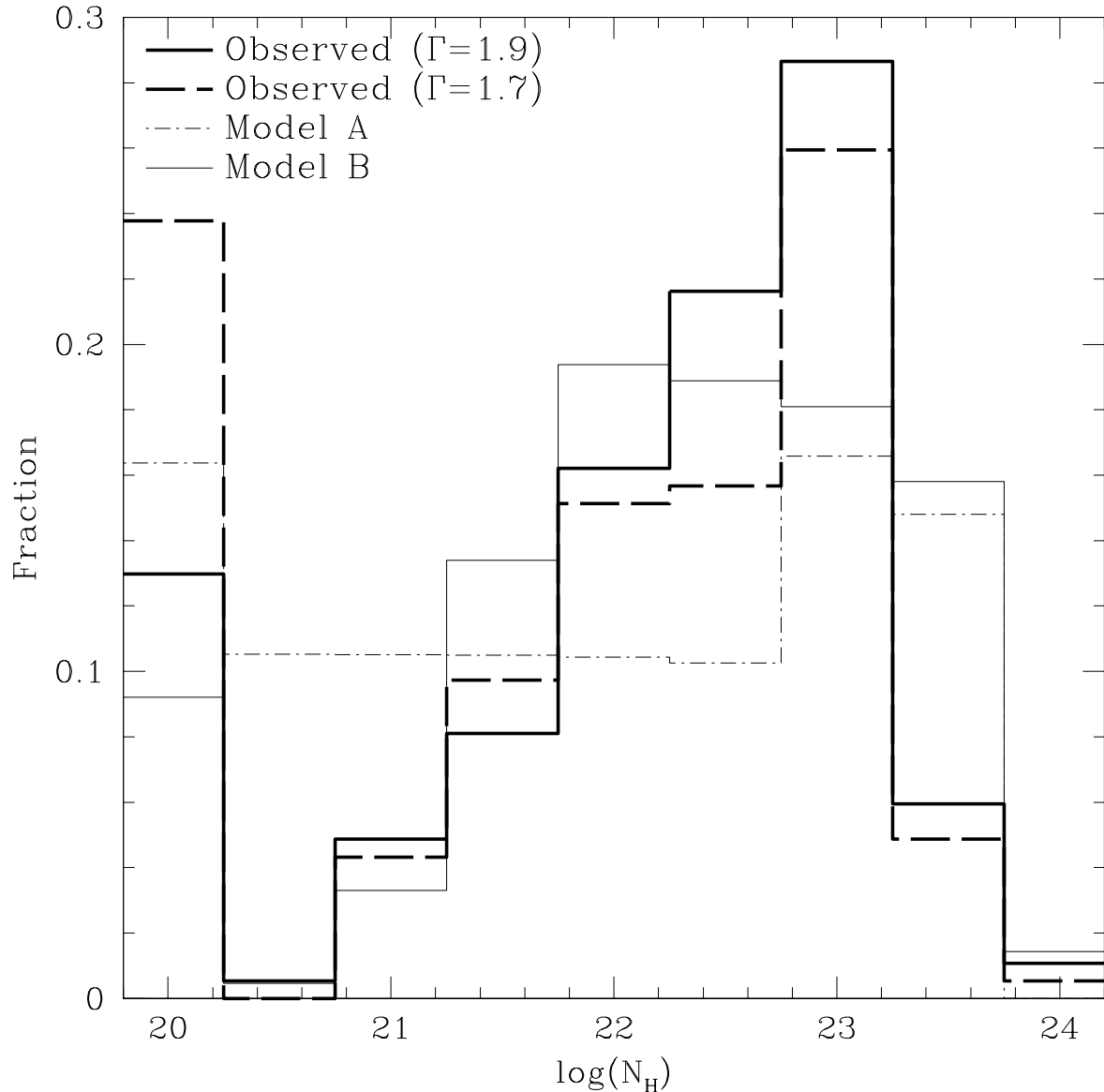


Fig. 3.— Distribution of intrinsic obscuring column density for X-ray sources in the GOODS fields with spectroscopic redshifts. The N_H values were derived assuming an intrinsic power-law spectrum with photon index $\Gamma = 1.9$ (solid line) or $\Gamma = 1.7$ (dashed line) and photoelectric absorption cross sections given by Morrison & McCammon (1983), shifted to the rest frame using redshifts from (Szokoly et al. 2004). Dashed-dotted line: N_H distribution of U03 (model A). Light solid line: N_H distribution calculated assuming a simple unified model with a dust torus geometry for the obscuring material and the GOODS flux limit (model B). As can be seen in this plot, model B (which is physically motivated) provides a good fit to the observed sources in the GOODS fields, apart from the expected incompleteness at high column densities.

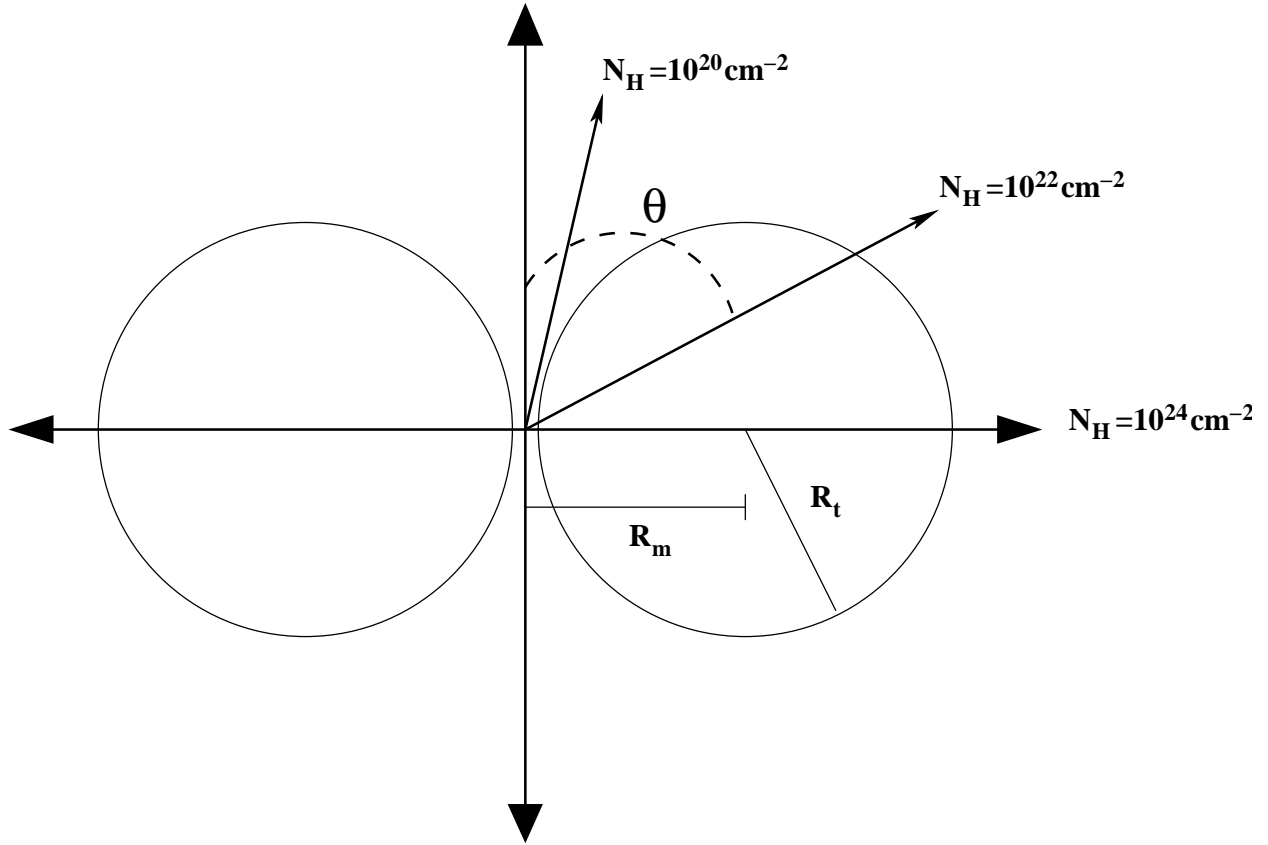


Fig. 4.— Schematic diagram of the AGN torus model used to calculate the intrinsic N_H distribution expected for a random orientation. In this plot R_m is the distance from the black hole to the center of the torus and R_t is the radius of obscuring material. The torus parameters are chosen so that equatorial lines of sight correspond to column densities of $N_H = 10^{24} \text{ cm}^{-2}$ and polar lines of sight have obscuration comparable to or less than typical Galactic values, $N_H \sim 10^{20} \text{ cm}^{-2}$.

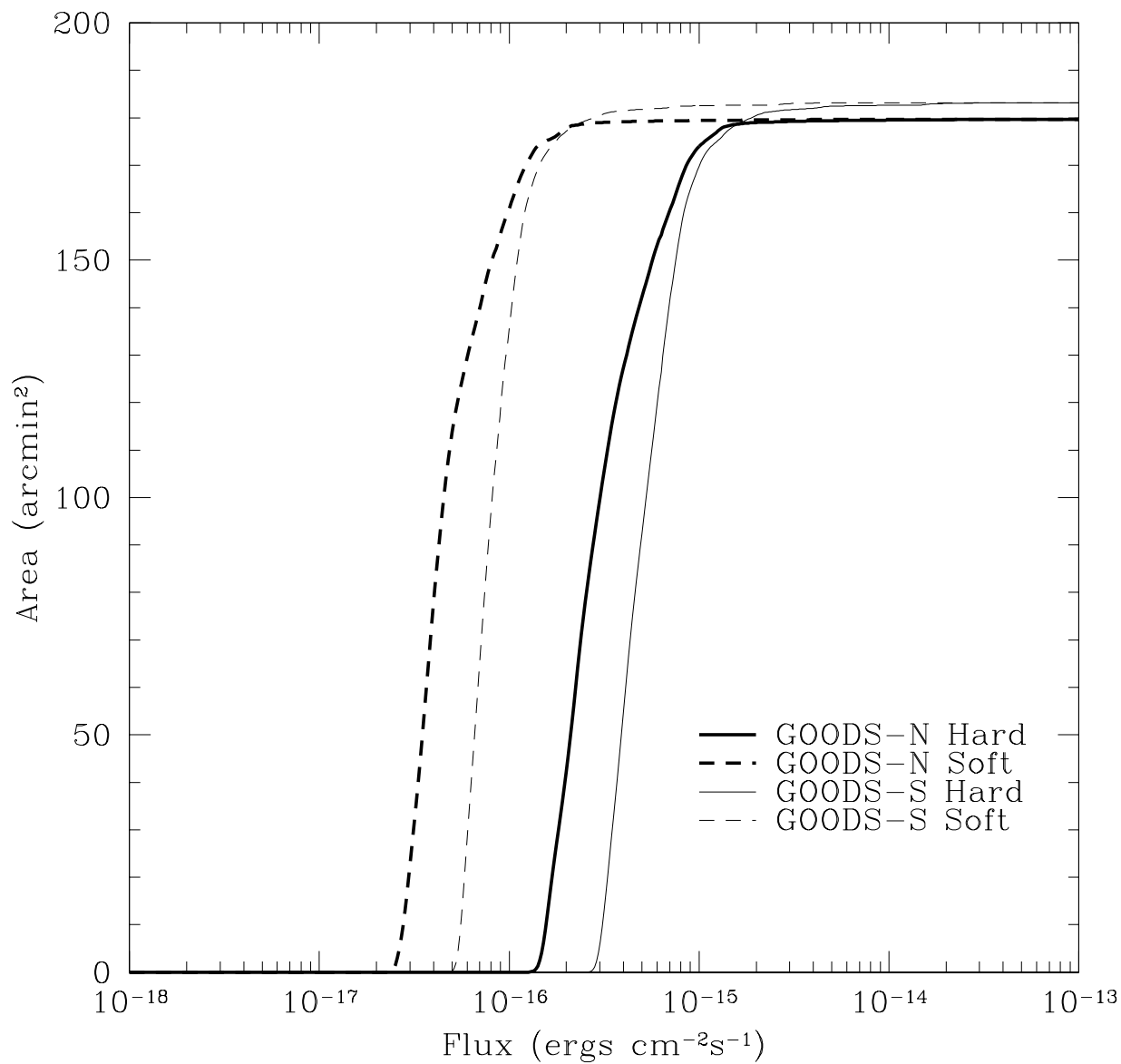


Fig. 5.— Area covered as a function of depth reached in the GOODS North (2 Ms) and South (1 Ms) fields with the *Chandra* X-ray observatory, based on the calculation presented in A03 over only the GOODS regions. This covered area as a function of depth was used in the subsequent calculation of expected number counts.

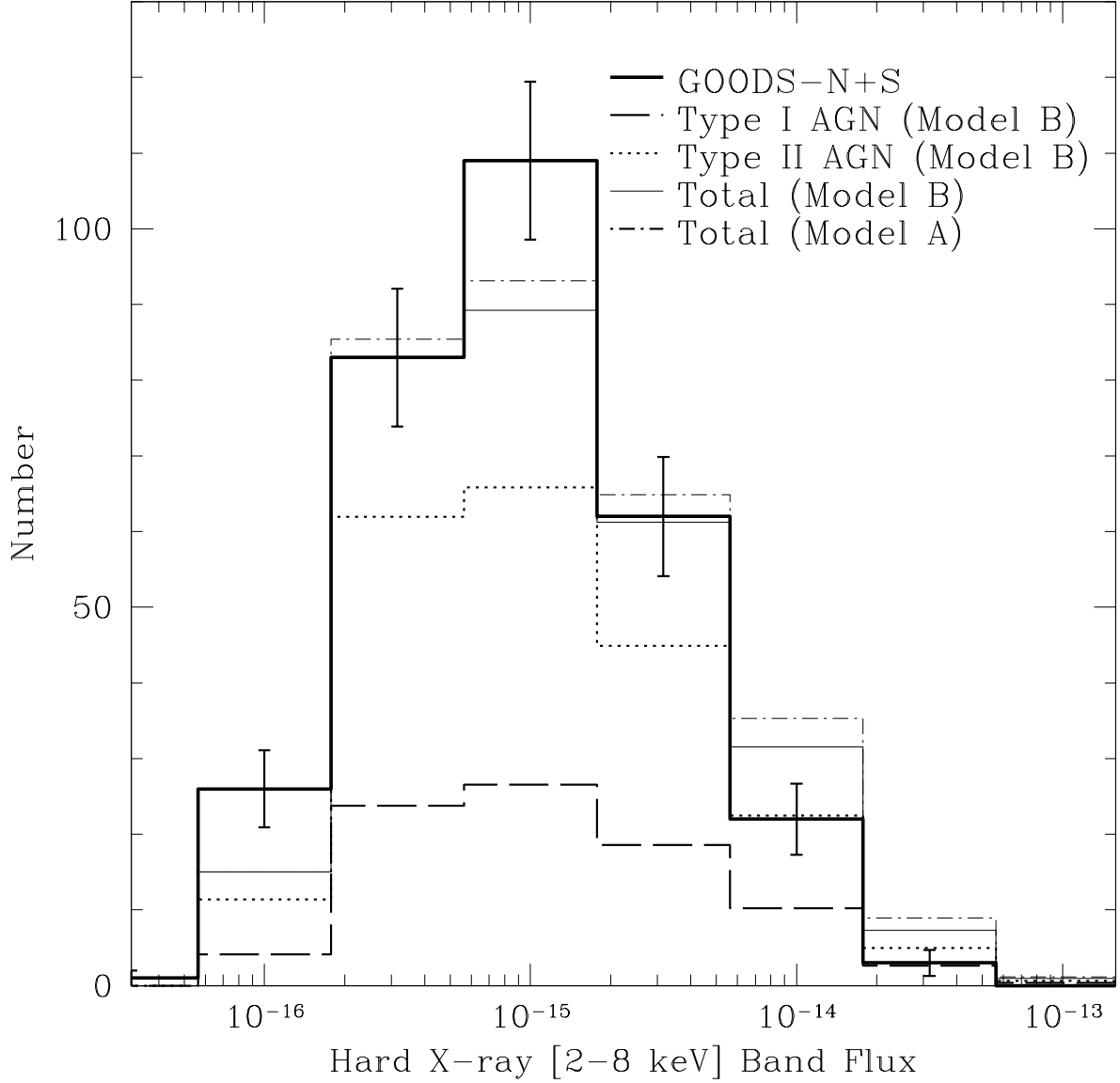


Fig. 6.— Hard X-ray flux (2-8.0 keV) distribution for the entire sample of hard X-ray detected sources in the GOODS-North and -South fields (*heavy solid line*, sources with or without spectroscopic redshifts), compared to the number counts calculated from the hard X-ray luminosity function and models A (*dot-dashed line*) and B (*light solid line*), with the individual contributions of unobscured (Type 1) (*dashed line*) and obscured (Type 2) (*dotted line*) AGN shown separately. Note that Type 1 and Type 2 AGN follow similar distributions, as expected from the unified model, since hard X-rays are not strongly affected by absorption.

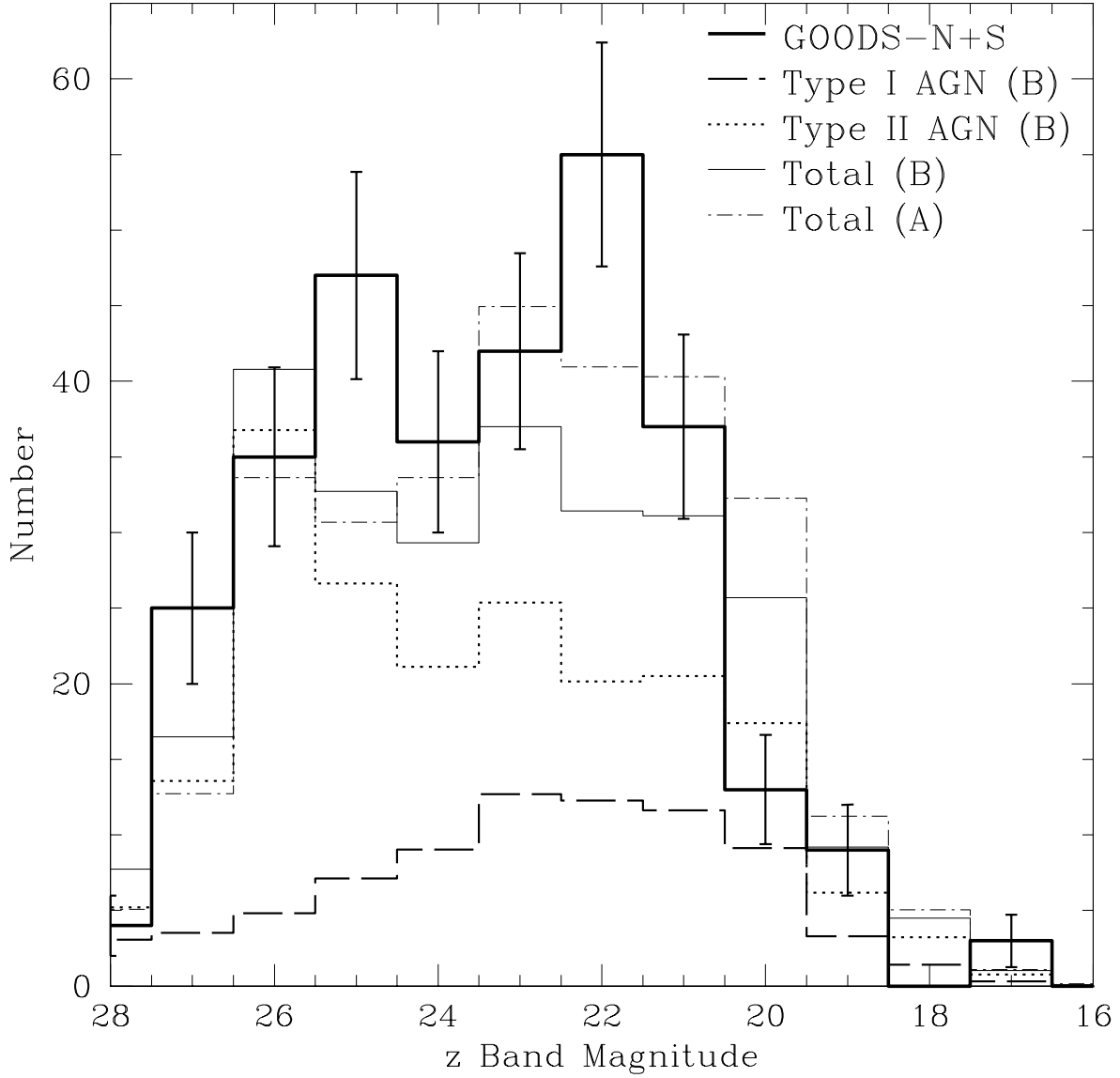


Fig. 7.— Distribution of observed z -band magnitudes for the entire sample of GOODS-North and GOODS-South X-ray sources (*heavy solid line*), compared to the summed distribution of all the sources in model A (*dot dashed line*) and model B (*light solid line*). The distribution of unobscured (Type 1) (*dashed line*) and obscured (Type 2) (*dotted line*) AGN calculated using model B is also shown. The agreement is very good (K-S test gives 71% for model B and 53% for model A), showing that in a hard X-ray luminosity function both obscured and unobscured AGN are well represented. In the unified model (model B), the bright end of the distribution includes both Type 1 and Type 2 AGN, while the faint end is dominated by Type 2 AGN, as expected from the obscuration of the optical emission of the central engine. In all cases, most of the optical emission for Type 2 AGN comes from the host galaxy.

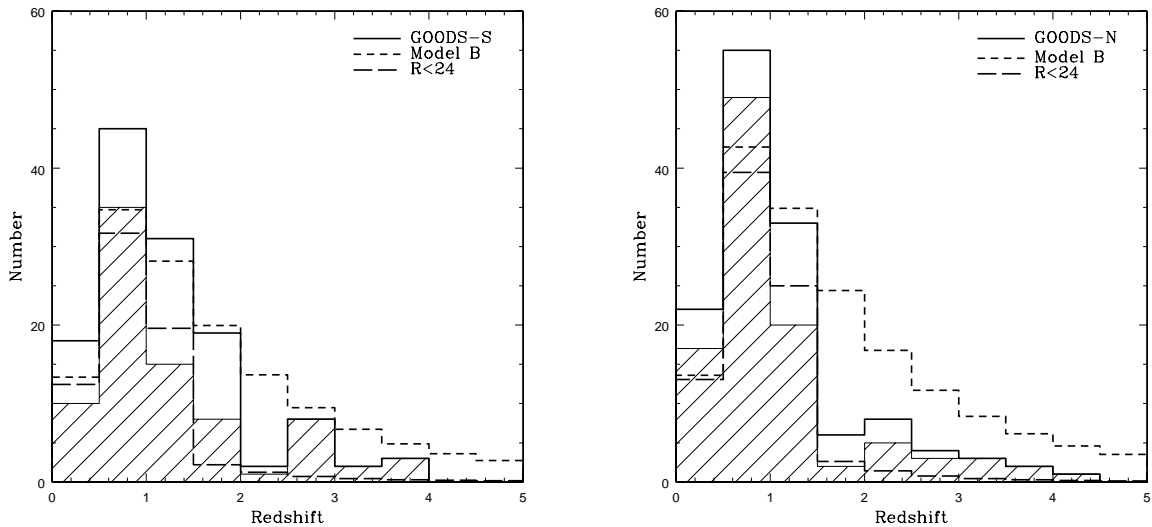


Fig. 8.— Redshift distributions for AGN in the GOODS-South (left panel) and North (right panel) fields. The observed redshift distribution (*heavy solid line*) includes both spectroscopic (*hatched area*) and photometric redshifts and is 100% complete in the GOODS-S field and 75% complete in the GOODS-N region. The expected distribution (*dashed line*) for the complete AGN population detected in X-rays, calculated from our models (it is indistinguishable for models A and B), is similar but has more AGN at high redshift, especially compared to the distribution of spectroscopic redshifts. The distribution for sources with $R < 24$ mag (*long dashed line*) is very similar to the observed distribution of sources with spectroscopic redshifts. The discrepancy is larger in the GOODS-N field because of incompleteness in the redshifts. Spectroscopic redshifts are limited to AGN with $R < 24$ mag and thus exclude the high-redshift obscured AGN in the model, a larger fraction of which are included in the photometric-redshift sample. The data are therefore consistent with a significant high-redshift population of obscured AGN which are missed in spectroscopic samples due to a selection effect.

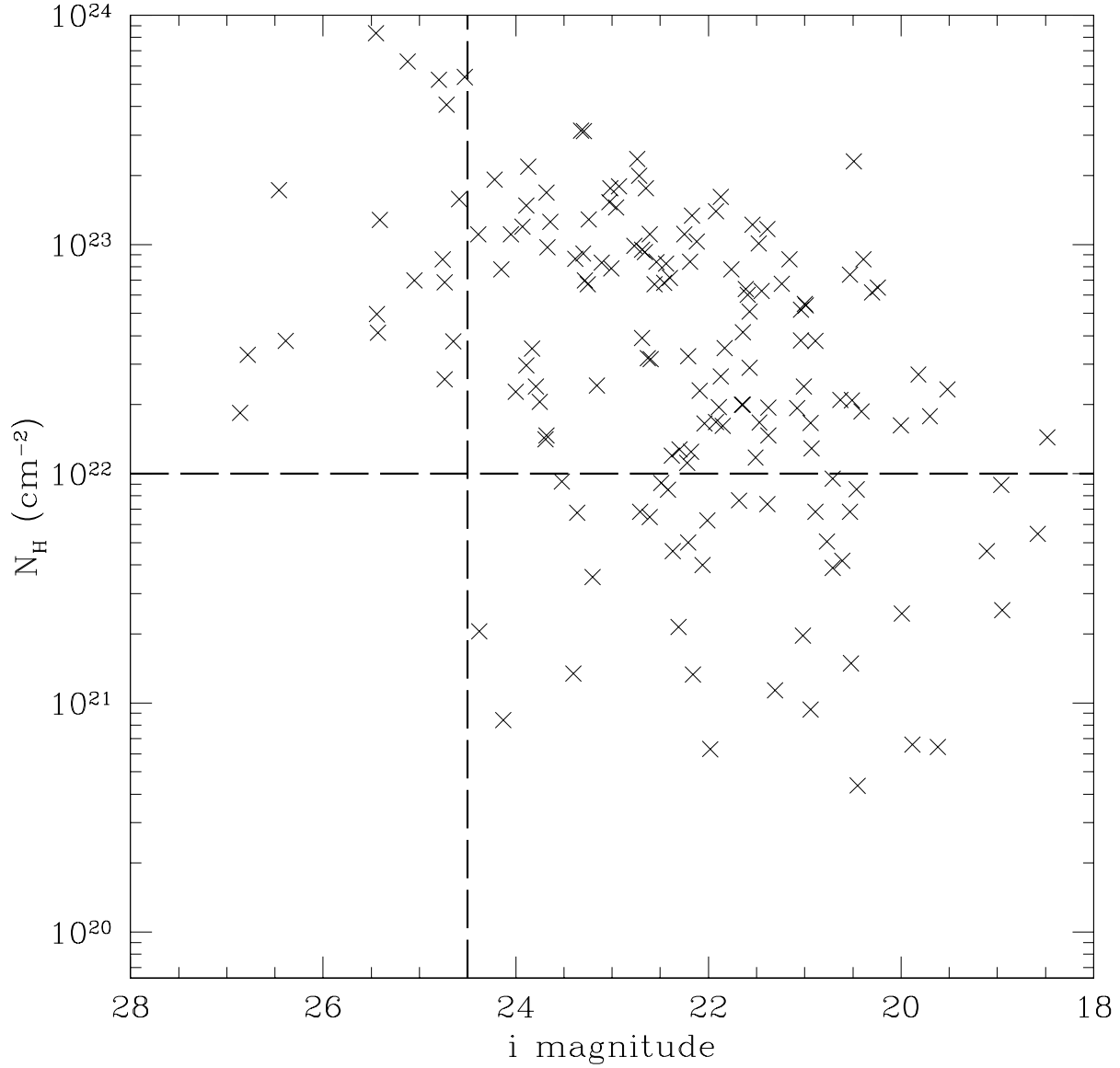


Fig. 9.— Neutral hydrogen column density versus i -band magnitude for X-ray sources with redshifts in the GOODS-South and -North fields. The N_H values were derived assuming an intrinsic power-law spectrum with photon index $\Gamma = 1.9$ and photoelectric absorption cross sections given by Morrison & McCammon (1983), shifted to the rest frame using spectroscopic redshifts from Szokoly et al. (2004) and Barger et al. (2003). The horizontal line at $N_H = 10^{22} \text{ cm}^{-2}$ separates Type 1 (unobscured) and Type 2 (obscured) AGN. The vertical line at $i = 24.5$ marks the spectroscopic limit for most cases. Given the spread in the intrinsic luminosity of the AGN and the constant contribution of an unreddened host galaxy, the correlation between N_H and i magnitude is weak. However, a general trend can be seen, with bright optical sources tending to be unobscured while those with higher values of N_H are fainter in the optical. Also, no Type 1 AGN is observed at magnitudes dimmer than $i \simeq 24$, consistent with the predictions of our model (see Fig. 7).

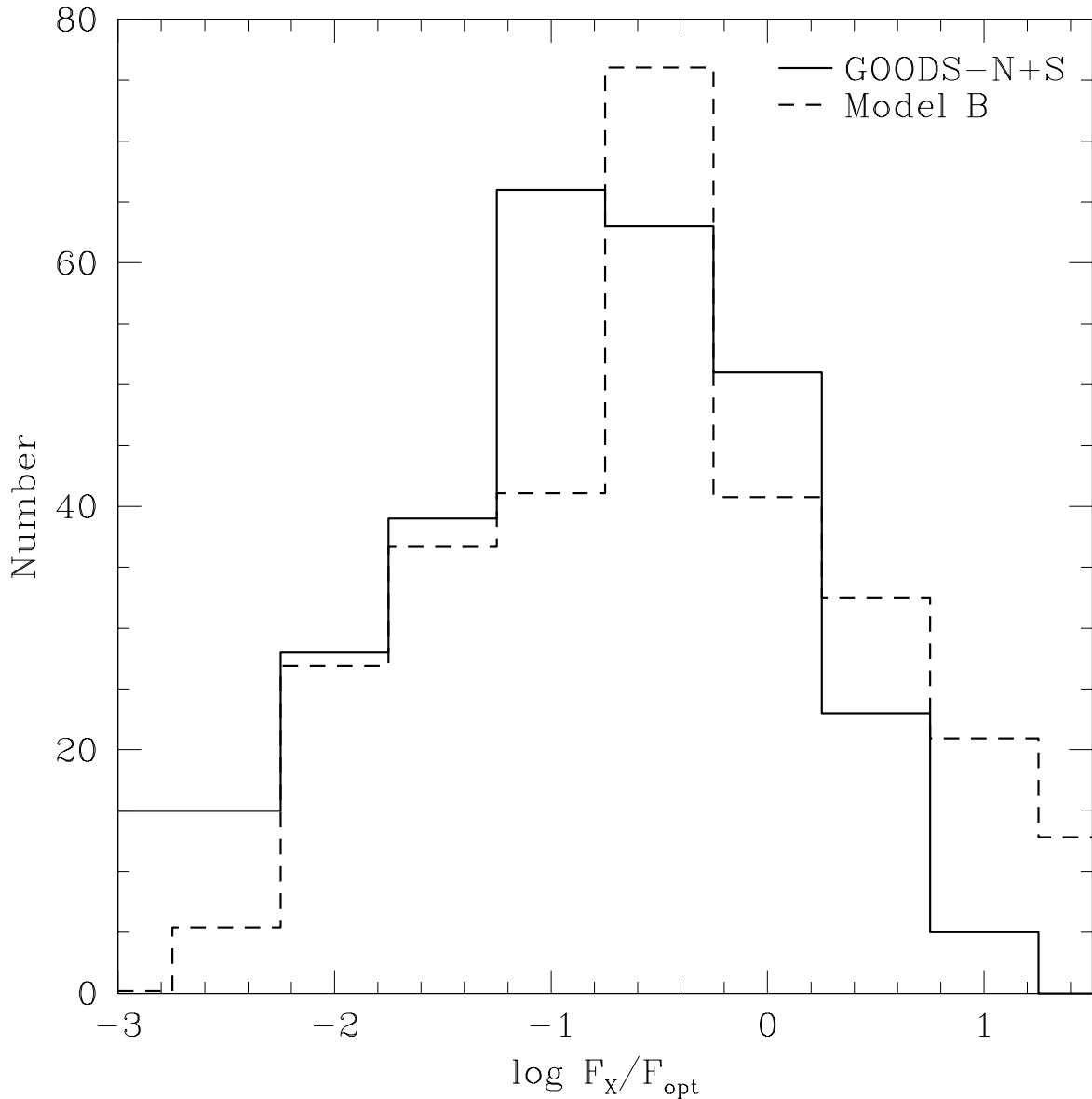


Fig. 10.— X-ray-to-optical flux ratio distribution for sources in the GOODS-North and -South fields (solid line) compared to the predicted distribution of model B (dashed line). The X-ray flux is calculated in the (0.5-8 keV) band in the observed frame and is not corrected for obscuration. Optical flux is calculated from the z -band magnitude. Both distributions are very similar, except at the extremes. At low F_X/F_{opt} non-AGN X-ray sources, mainly starburst galaxies, contribute to the observed distribution, while at the high F_X/F_{opt} , the most obscured AGN in the model are missing from the X-ray surveys.

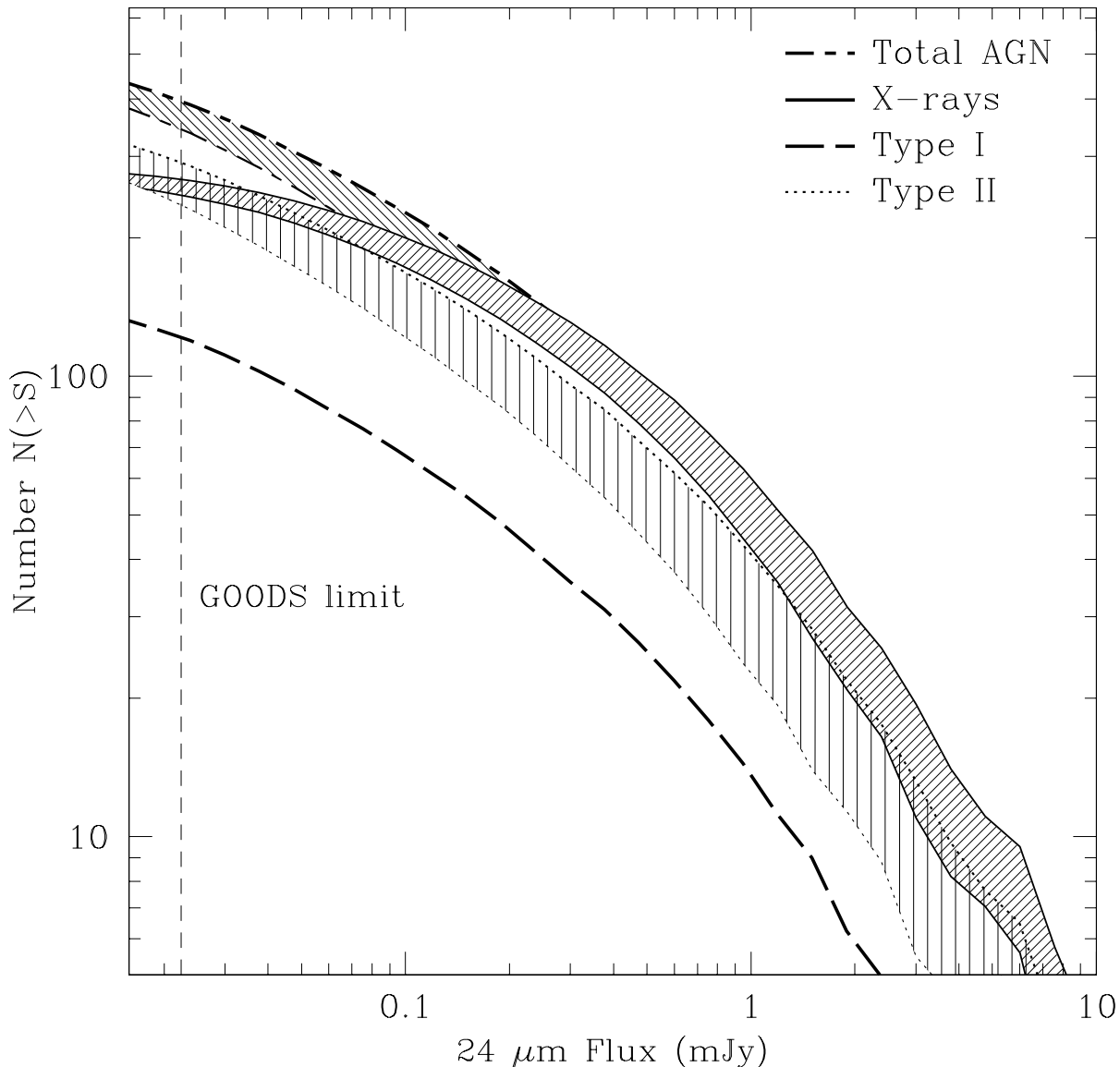


Fig. 11.— Predicted AGN number counts at $24\mu\text{m}$ for the total area and depth expected in the GOODS *Spitzer* Legacy fields (0.08 deg^2). (*long-short dashed line:*) total AGN counts; (*dashed line:*) unobscured AGN; (*dotted line:*) obscured AGN; (*solid line:*) X-ray detected sources. For total and obscured counts, the lower line correspond to the infrared dust emission model with parameters $R_i/R_o = 30$ and $q = 1$, while the upper line was obtained using $R_i/R_o = 30$ and $q = 2$. A third model with $R_i/R_i = 100$, $q = 2$ was also used and the results are between the other two models. For unobscured sources, our results are independent of the model used, which reflects the small dependence of the IR emission on the details of the torus composition and geometry for sources in which the line of sight does not intercept it. A significant number of the total AGN in the field, roughly 50% at the GOODS $24\text{-}\mu\text{m}$ flux limit, are not detected by *Chandra* in X-rays. Most of these sources are obscured AGN with $N_H > 10^{23} \text{ cm}^{-2}$.

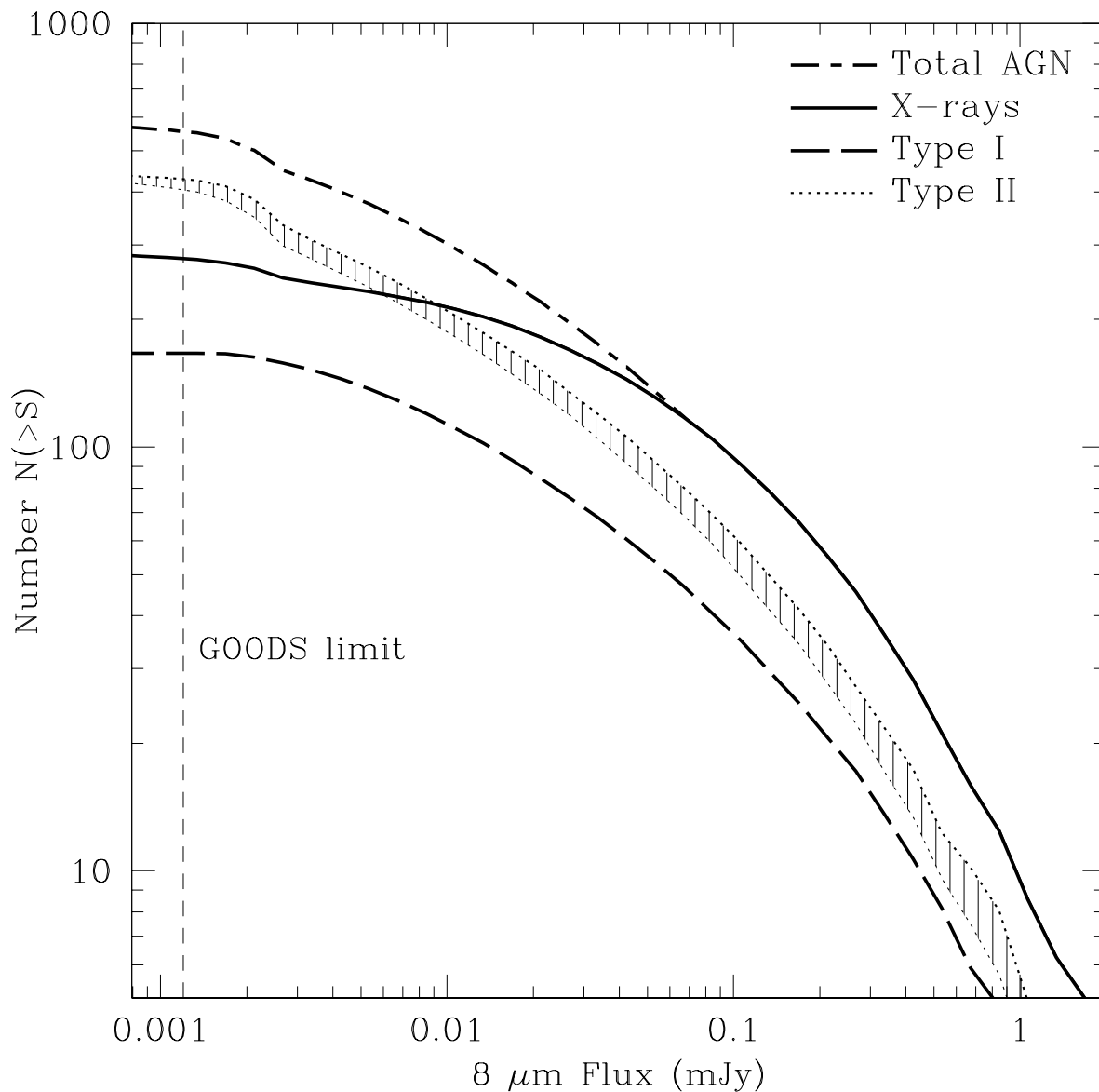


Fig. 12.— Same as Figure 11, but for the $8\text{-}\mu\text{m}$ IRAC band. In this case, for the total X-ray counts just one infrared model ($R_i/R_o = 30, q = 1$) was used since the difference with other parameters was small. Again, roughly 50% of the predicted *Spitzer* sources at the flux limit are not detected in the current *Chandra* deep fields.

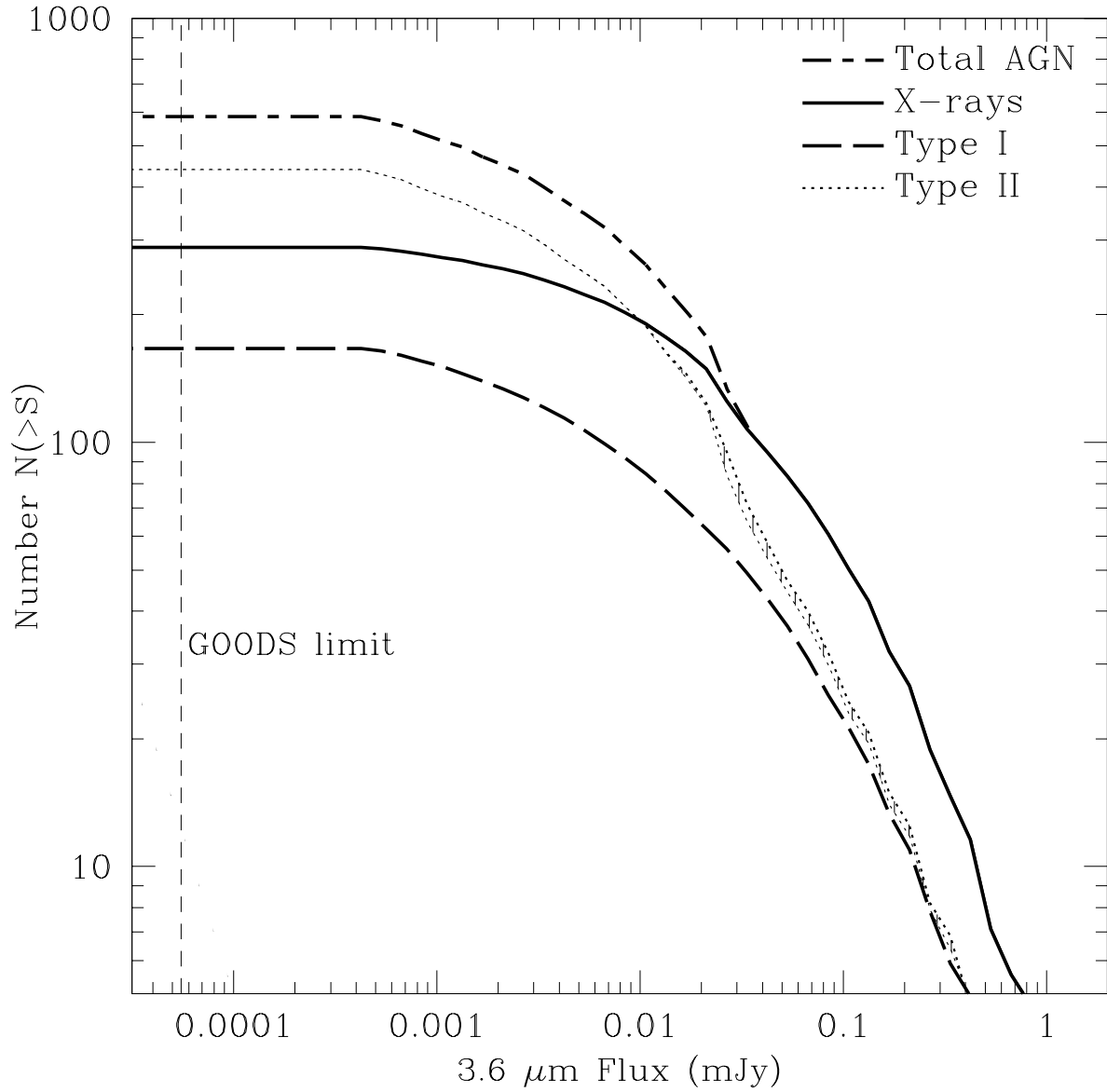


Fig. 13.— Same as Figure 11, but for the 3.6- μm IRAC band. About 50% of the predicted *Spitzer* sources are missed in X-rays at the GOODS flux limit.